Parallel Direct Numerical Simulation of 3D Interface-Resolved Droplet Evaporation

by

Abay Kozhabergenov

A Dissertation Submitted to the
Graduate School of Sciences and Engineering
in Partial Fulfillment of the Requirements for
the Degree of

Master of Science

in

Mechanical Engineering

KOÇ ÜNİVERSİTESİ

January 12, 2024

Parallel Direct Numerical Simulation of
3D Interface-Resolved Droplet Evaporation

Koç University

Graduate School of Sciences and Engineering

This is to certify that I have examined this copy of a master's thesis by

Abay Kozhabergenov

and have found that it is complete and satisfactory in all respects,
and that any and all revisions required by the final
examining committee have been made.

Committee Members:

_____

Prof. Dr. Metin Muradoğlu (Advisor)

_____

Prof. Dr. Hasan Bedir

_____

Prof. Dr. Murat Sözer

Date: _____

To Allah, my mother and my brother.

ABSTRACT

Parallel Direct Numerical Simulation of
3D Interface-Resolved Droplet Evaporation
Abay Kozhabergenov
Master of Science in Mechanical Engineering
January 12, 2024

Multi-phase flows and phase transitions are widely observed phenomena in natural processes and engineering applications such as atmospheric precipitation, bubbles forming during water boiling, and spray combustion. To study the physics of such phenomena and to broaden their application areas, simulations of multi-phase flows with phase change are crucial. Therefore, in this thesis, a parallel front-tracking/finite-difference method is developed for interface-resolved fully 3D simulations of droplet evaporation. In this method, the mass, momentum, and energy conservation equations are solved on a 3D-Cartesian, uniform, fixed, staggered Eulerian grid while a Lagrangian grid is employed to track the interface between the liquid and vapor phases. The method is first validated for the classical d^2-law. Then the method is applied to simulate the evaporation of a 3D Leidenfrost droplet.

ÖZETÇE

Arayüzü Çözümlenir Olan Üç Boyutlu Damlacık Buharlaşmasının Paralel Doğrudan Sayısal Simülasyonu

Abay Kozhabergenov

Makine Mühendisliği, Yüksek Lisans

12 Ocak 2024

Çoklu fazlı akışlar ve faz geçişleri dünya genelinde yaygın olarak gözlemlenen olaylardır; bunlardan bazıları şunlardır: atmosferik yağış, su kaynadığında oluşan baloncuklar, sprey yanması. Dolayısıyla bu fiziksel olayların incelenmesi ve uygulama alanlarını genişletmek amacıyla çok fazlı akışların ve faz değişikliklerinin simülasyonu önemli bir araştırma konusu haline gelmiştir. Bu doğrultuda, üç boyutlu iki fazlı sistem simülasyonları için bir paralel arayüz izleme/sonlu fark yöntemi, enerji için korunma denklemlerini tanıtarak ve sıcaklık gradyanı tarafından sürülen bir faz değişimi modelini tutarlı bir şekilde iki tür çözüm ağı kullanılarak geliştirilmiştir. Yöntemin sonlu fark bileşeni, üç boyutlu Kartezyen, tekdüze, sabit, sıralı Euleryen çözüm ağında bir skalar sıcaklık alanını evrimleştirmektedir. Aynı zamanda, arayüz izleme bileşeni, ısıl ve kütle transferine bağlı olarak fazlar arasındaki değişikliklere cevap vererek, üç boyutlu tekdüze ve sabit olmayan Lagrangyan çözüm ağındaki arayüzü dinamik bir şekilde çözmektedir. Sıcaklık alanının evrimi ve damlacık buharlaşması için uygulanan sayısal yöntemler, çözüm ağı uyum çalışmaları ile ısıl denklemin analitik çözümüne ve teorik d^2-yasasına karşı etkili doğrulama süreçlerinden geçmiştir. Geliştirilmiş sayısal yöntem, üç boyutlu Leidenfrost damlacığının buharlaşması problemine başarıyla uygulanmıştır. Bu da çeşitli iki fazlı akışların faz geçişini içeren simülasyonların gerçekleştirilmesine olanak tanımaktadır.

ACKNOWLEDGMENTS

I would like to acknowledge and give my greatest thanks to my advisor Professor Dr. Metin Muradoğlu who made this work possible. I want to thank all my family and friends for supporting me in this stage of my life.

TABLE OF CONTENTS

LIST OF FIGURES

Chapter 1

INTRODUCTION

A falling raindrop resulting from condensed water vapor in the atmosphere, a rising gas bubble nucleated in boiling liquid, flowing blood in vessels and air in the lungs of living organisms, floating oil drops on a heated pan, a spreading pyroclastic cloud produced during the volcanic eruption are just a few examples of *multi-phase flows* that were already being studied back in the 19th century by Besant (1859), have been widely investigated in the 20th century [Rayleigh (1917), Plesset and Zwick (1954), Mikic et al. (1970), Prosperetti and Plesset (1978), Lee (1993)], and successfully utilized in petroleum industry [Larson et al. (1981)], geophysical [Olbricht (1996)] and biological processes [Groberg (2001)], spray combustion [Clift et al. (2005)] and heat flux electronic devices [Ammerman et al. (1996)], and aerospace applications [Kamakoti and Shyy (2004)]. Simulations of multiphase flows receive more and more interest nowadays, driven by a wide range of scientific and engineering applications.

A captivating to simulate instance of multi-phase flows is the Leidenfrost effect, which was named after its discoverer Leidenfrost (1756) and has been applied for spray cooling [Kim (2007)], spray deposition Attinger et al. (2000), and spray combustion [Moreira et al. (2010)]. This phenomenon unveils itself when a liquid droplet encounters a surface with a temperature significantly surpassing its boiling point. The Leidenfrost effect is not merely a physical event but a complex interplay of thermodynamics, fluid dynamics, and surface interactions, yielding a mesmerizing suspension of the droplet above the hot surface that makes it a compelling subject for scientific investigation in the fundamental understanding of the behavior of liquid droplets on superheated surfaces along with spanning and advancing its practical applications.

However, the presence of an interface undergoing dimensional, geometrical, and topological changes, that produce sharp gradients through phases, as well as the occurrence of phase change, that introduces an additional level of complexity, both intensify challenges associated with the modeling of multi-phase flows or, as also referred to, interfacial flows.

Acknowledgingly, the escalating computational capabilities have established Direct Numerical Simulation (DNS) as a promising technique for simulating and analyzing system designs across a broad spectrum of operating parameters. Particularly, as micro and nano-scale applications gain prominence, DNS has emerged as an efficient tool for enhancing system designs and overcoming the limitations of experimentation [Woerner (2012)]. Therefore, alongside theoretical and experimental analyses to study interfacial flows with phase change, different numerical methods have been developed that can be considered in two groups. The first group analyzes fluid-structure interaction [Mittal and Iaccarino (2005)] where a fluid meets a solid material. In the second group (into which this thesis falls), a domain that contains two interfacing phases of the same fluid (for example, water and its vapor) or different fluids (for example, air and water), in other words, a gas-liquid flow is analyzed that, in turn, can be modeled using a two-fluid formulation [Drew (1983), Ishii (1987), Drew and Lahey (1993), Zhang and Prosperetti (1994)] and a one-fluid formulation that takes into account phase change i.e., evaporation or condensation. The main advantage of the latter formulation, as well as the reason for its usage in this thesis, is that only a single set of mathematical equations is solved for both phases instead of two sets as in the former one.

Harlow and Welch (1965) introduced one of the first approaches for simulating free surface flows known as the marker and cell (MAC) method. In this technique, marker particles are distributed throughout the fluid region, moving with the local fluid velocity, thereby defining the shape and location of the interface at the current time. Hirt and Nichols (1981) proposed a memory-efficient region-following scheme, termed the volume of fluid (VOF) method, where a single fluid volume fraction value is assigned to each mesh cell, minimizing the number of marker particles

per cell. Karl et al. (1996) are among the first researchers who employed the VOF method to model the behavior of an evaporating, non-wetting droplet touching a hot wall. The impact of vapor velocity on fluid flow was disregarded in their simulation. Harvie and Fletcher (2001) utilized the VOF method to develop an axisymmetric code specifically for simulating droplet evaporation on a hot plate. In their model, they incorporated a one-dimensional representation of heat transfer within the vapor film between the plate and the liquid droplet. To investigate a horizontal film boiling problem, Welch and Wilson (2000) opted for the VOF method. Schlottke and Weigand (2008) delved into a comprehensive numerical simulation of a 3D evaporating and significantly deformed droplet, employing the VOF method. The interface is alternatively conceptualized as a level set function, successfully implemented by various researchers for simulating multiphase flows [Osher and Sethian (1988), Sussman et al. (1994)]. To maintain the continuity and resolution of the level set function, it is preserved as a signed distance function throughout the simulation without the need for interface reconstruction [Sussman et al. (1994)]. Film boiling scenarios were scrutinized by Son and Dhir (1998) and Gibou et al. (2007) using the Level Set method. Tanguy et al. (2007), incorporating the ghost fluid method [Fedkiw et al. (1999)], utilized the Level Set method to simulate the evaporation of a dynamic and deformable droplet. Meanwhile, Ge and Fan (2006) applied the level set method to simulate the impact of a saturated liquid drop on a heated surface, revealing that an increase in sub-cooling leads to a decrease in the Leidenfrost degree. Chatzikyriakou et al. (2009) and Pournaderi and Pishevar (2012) used the level set method to accurately capture the interface to solve the Navier–Stokes equations for a droplet interacting with a superheated wall. Additionally, the concept of a diffuse interface has been tested to verify its capability of modeling two-phase flows [Anderson et al. (1998), Jacqmin (1999)]. The lattice Boltzmann method stands out as another promising numerical approach for modeling multiphase flow. Safari and colleagues integrated phase change models based on temperature [Safari et al. (2013)] and species gradient [Safari et al. (2014)] into the lattice Boltzmann method, which was originally developed by Lee (2009). Karami et al. (2017) explored the effects

of diverse non-dimensional parameters on a 2D droplet at the Leidenfrost regime. These methods collectively enter the category of interface-capturing methods.

Another category, referred to as interface-tracking methods, involves representing the interface with a separate Lagrangian grid while solving the governing equations on an Eulerian grid. In some earlier implementations, the moving interface was tracked by modifying the background Eulerian grid near the interface to align with it [Glimm et al. (1981), Glimm et al. (1981), Glimm and McBryan (1985)]. Unverdi and Tryggvason (1992) and Tryggvason et al. (2001) introduced a front-tracking method for isothermal multifluid flows that eliminates the need for any re-meshing of the background grid to track the interface. Instead, the interface or front is explicitly tracked by interpolating the velocity field from the Eulerian grid onto the interface marker points. The front-tracking technique has undergone expansions by several researchers to encompass mass transfer and phase change phenomena. Juric and Tryggvason (1998), for instance, conducted simulations of film boiling, employing an iterative process to establish the accurate temperature boundary condition at the interface. This iterative algorithm was also utilized by Qian et al. (1998) to track the flame front of a premixed flame. Esmaeeli and Tryggvason (2003) and Esmaeeli and Tryggvason (2004) eliminated the need for the iterative algorithm by setting the interface temperature as the saturation temperature at the system pressure.

The contribution of this thesis is an advancement of a numerical method, precisely, a parallel front-tracking/finite-difference method for multi-phase system simulations fully parallelized by Farooqi et al. (2019). The conservation equations for energy considering a temperature gradient-driven phase change model [Irfan and Muradoglu (2017)] are coupled and computed consistently. The finite-difference part of the method implemented to calculate scalar fields is used appropriately to evolve a scalar temperature field in a 3D-Cartesian, uniform, fixed, staggered Eulerian grid, while the front-tracking part resolves the interface regarding its changes due to heat and mass transfer between phases on a 3D unstructured Lagrangian grid. The numerical method for temperature field evolution and droplet evaporation are successfully verified by grid-convergence and validated with the heat equation and

the theoretical d^2-law, correspondingly. Ultimately, the advanced numerical method is tested by evaporation of a 3D Leidenfrost droplet floating above a heated surface, and thus it allows us to simulate different kinds of two-phase flows involving phase transition.

The composition of this thesis is as follows: after the introduction in Chapter 1, a mathematical model with its assumptions, governing equations for conservation laws, and non-dimensional flow parameters is formulated in Chapter 2. Upon it, Chapter 3 explains the numerical implementation of gas-liquid flow simulations, results and discussion of which are presented in Chapter 4. The thesis work is concluded in Chapter 5 and its list of references in alphabetical order is provided at the end.

Chapter 2

MATHEMATICAL FORMULATION

In this chapter, the mathematical formulation is described for a gas-liquid flow where a liquid droplet is evaporating in a bulk gaseous substance, and it starts with stating the theoretical assumptions made throughout simulations.

2.1 Assumptions

i. The flow is assumed to be *incompressible*.

$$\nabla \cdot \mathbf{u} = 0 \tag{2.1}$$

ii. Fluids are assumed to have *constant* intensive properties, namely, *densities*, *dynamic viscosities*, *specific heat capacities*, and *thermal conductivities* as expressed in Eq. 2.2 to Eq. 2.5, respectively.

$$\frac{\mathrm{D}\rho}{\mathrm{D}t} = \frac{\partial \rho}{\partial t} + \mathbf{u} \cdot \nabla \rho = 0 \tag{2.2}$$

$$\frac{\mathrm{D}\mu}{\mathrm{D}t} = \frac{\partial \mu}{\partial t} + \mathbf{u} \cdot \nabla \mu = 0 \tag{2.3}$$

$$\frac{\mathrm{D}c_p}{\mathrm{D}t} = \frac{\partial c_p}{\partial t} + \mathbf{u} \cdot \nabla c_p = 0 \tag{2.4}$$

$$\frac{\mathrm{D}k}{\mathrm{D}t} = \frac{\partial k}{\partial t} + \mathbf{u} \cdot \nabla k = 0 \tag{2.5}$$

iii. Last but not least, the interface between phases is assumed to be infinitesimally thin, and material properties vary discontinuously across the interface as it is illustrated in 2.1. In the present *one-fluid formulation*, each phase is identified

by an indicator function defined as

$$I(\mathbf{x},t) = \begin{cases} 1 & \text{inside the interface} \\ 0 & \text{outside the interface} \end{cases} \tag{2.6}$$

The indicator function can be expressed mathematically as [Tryggvason et al. (2001), Frigo and Johnson (2005)].

$$\nabla I(\mathbf{x},t) = -\int_A \hat{\mathbf{n}}\,\delta(\mathbf{x}-\mathbf{x}_f)\,\mathrm{d}A_f \tag{2.7}$$

where $\hat{\mathbf{n}}$ is the unit normal vector at the interface, $\mathbf{x}_f$ is the point at the interface, $\delta(\mathbf{x}-\mathbf{x}_f)$ is the Dirac delta function, and A_f is the area of the interface. Considering the first two assumptions, the material properties within the gas-liquid flow domain can be defined in terms of the indicator function as given in Eq.2.8 to Eq.2.11.

$$\rho = \rho_l\, I(\mathbf{x},t) + \rho_g(1 - I(\mathbf{x},t)) \tag{2.8}$$

$$\mu = \mu_l\, I(\mathbf{x},t) + \mu_g(1 - I(\mathbf{x},t)) \tag{2.9}$$

$$c_p = c_{p,l}\, I(\mathbf{x},t) + c_{p,g}(1 - I(\mathbf{x},t)) \tag{2.10}$$

$$k = k_l\, I(\mathbf{x},t) + k_g(1 - I(\mathbf{x},t)) \tag{2.11}$$

These assumptions allow us to represent the gas-liquid flow using a coupled system of governing equations for mass, momentum, and energy conservation in a differential convective form, as detailed in the next section.

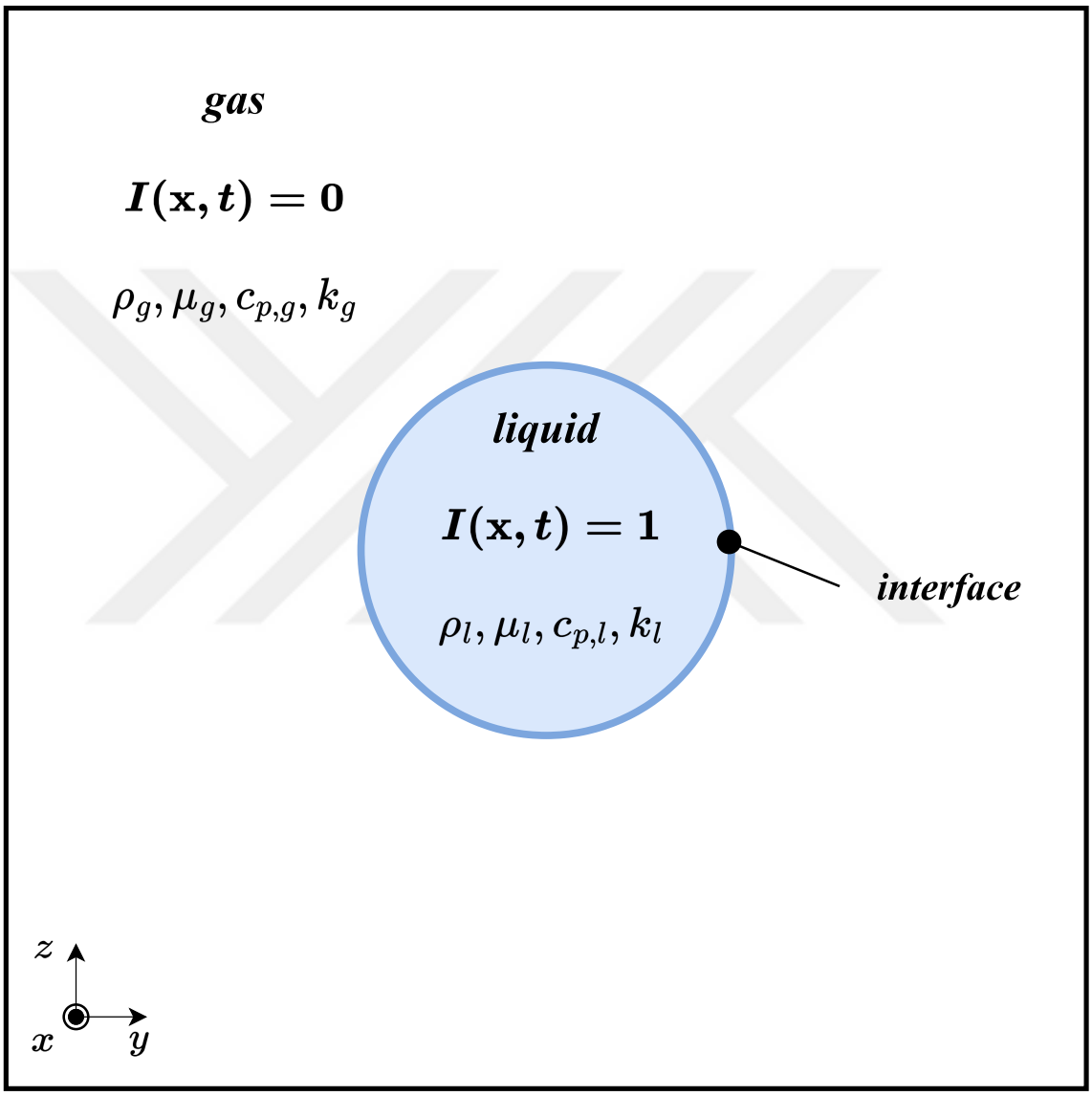

Figure 2.1: Mathematical one-fluid formulation for a gas-liquid flow domain with different material properties.

2.2 Governing equations

2.2.1 Conservation of mass

In the absence of phase change, the mass conservation equation can be written as

$$\frac{\partial \rho}{\partial t} + \nabla \cdot \rho \mathbf{u} = 0 \tag{2.12}$$

Fo an incompressible flow, the mass conservation (Eq.2.12) is simplified to the divergence-free velocity field condition (Eq.2.13).

$$\nabla \cdot \mathbf{u} = 0 \tag{2.13}$$

To regard phase-transition, by substituting the density expression from Eq.2.8 into Eq.2.12:

$$\begin{aligned} \left[\rho_l \, I(\mathbf{x},t) + \rho_g (1 - I(\mathbf{x},t))\right] (\nabla \cdot \mathbf{u}) = 0 \\ \rho_l \, I(\mathbf{x},t)(\nabla \cdot \mathbf{u}) + \rho_g (1 - I(\mathbf{x},t))(\nabla \cdot \mathbf{u}) = 0 \end{aligned} \tag{2.14}$$

and subsequently, by splitting into phases (i.e., gas and liquid), a mass-flux rate through the interface is introduced in Eq.2.15.

$$\begin{cases} \rho_l \, I(\mathbf{x},t)(\nabla \cdot \mathbf{u}) = -\dot{m} \\ \rho_g (1 - I(\mathbf{x},t))(\nabla \cdot \mathbf{u}) = \dot{m} \end{cases} \tag{2.15}$$

The three-dimensional δ-function, with the difference between the cell and front coordinates as an argument, is utilized to obtain non-zero values for the mass-flux rate exclusively at the interface between phases as given in Eq.2.16.

$$\begin{cases} I(\mathbf{x},t)(\nabla \cdot \mathbf{u}) = -\dfrac{1}{\rho_l} \int_A \delta(\mathbf{x} - \mathbf{x}_f) \, \dot{m}_f \, \mathrm{d}A_f \\ -I(\mathbf{x},t)(\nabla \cdot \mathbf{u}) + \nabla \cdot \mathbf{u} = \dfrac{1}{\rho_g} \int_A \delta(\mathbf{x} - \mathbf{x}_f) \, \dot{m}_f \, \mathrm{d}A_f \end{cases} \tag{2.16}$$

The sum of the equations in Eq.2.16 yields a modified mass continuity equation (Eq.2.17) satisfying the mass jump at the interface.

$$\nabla \cdot \mathbf{u} = \left(\frac{1}{\rho_g} - \frac{1}{\rho_l}\right) \int_A \delta(\mathbf{x} - \mathbf{x}_f)\, \dot{m}_f \, \mathrm{d}A_f \tag{2.17}$$

2.2.2 Conservation of momentum

The differential convective form of the Navier-Stokes equations for momentum conservation in the incompressible flow is formulated in Eq.2.18.

$$\begin{aligned} \frac{\mathrm{D}\mathbf{u}}{\mathrm{D}t} &= \frac{\partial \mathbf{u}}{\partial t} + \mathbf{u} \cdot \nabla \mathbf{u} = \frac{\partial \mathbf{u}}{\partial t} + \nabla \cdot \mathbf{u}\mathbf{u} - \mathbf{u}(\nabla \cdot \mathbf{u}) \\ &= \frac{1}{\rho} \left\{ -\nabla p + \nabla \cdot \mu \left[\nabla \mathbf{u} + (\nabla \mathbf{u})^T\right] + \rho \mathbf{g} + \int_A \sigma_f \, \kappa \, \hat{\mathbf{n}} \, \delta(\mathbf{x} - \mathbf{x}_f) \, \mathrm{d}A_f \right\} \end{aligned} \tag{2.18}$$

The last terms on the left- and right-hand sides of Eq.2.18 handle the momentum jump employing Eq.2.17 and the surface tension acting just at the interface, respectively.

For 3D configuration, the momentum equations are written for velocity components in 3 directions in convective forms. The x, y, and z components of momentum conservation equation can be written as

$$\begin{aligned} &\frac{\partial u}{\partial t} + \frac{\partial u^2}{\partial x} + \frac{\partial uv}{\partial y} + \frac{\partial uw}{\partial z} - u\left(\frac{1}{\rho_g} - \frac{1}{\rho_l}\right)\dot{m}_f = \frac{1}{\rho}\left[\int_A \sigma_f \, \kappa \, \hat{\mathbf{n}} \, \delta(\mathbf{x} - \mathbf{x}_f) \, \mathrm{d}A_f \cdot \hat{\mathbf{i}} \right. \\ &\left. - \frac{\partial p}{\partial x} + \frac{\partial}{\partial x}\left(2\mu \frac{\partial u}{\partial x}\right) + \frac{\partial}{\partial y}\mu\left(\frac{\partial u}{\partial y} + \frac{\partial v}{\partial x}\right) + \frac{\partial}{\partial z}\mu\left(\frac{\partial u}{\partial z} + \frac{\partial w}{\partial x}\right) + \Delta\rho g_x\right] \end{aligned} \tag{2.19}$$

$$\begin{aligned} &\frac{\partial v}{\partial t} + \frac{\partial vu}{\partial x} + \frac{\partial v^2}{\partial y} + \frac{\partial vw}{\partial z} - v\left(\frac{1}{\rho_g} - \frac{1}{\rho_l}\right)\dot{m}_f = \frac{1}{\rho}\left[\int_A \sigma_f \, \kappa \, \hat{\mathbf{n}} \, \delta(\mathbf{x} - \mathbf{x}_f) \, \mathrm{d}A_f \cdot \hat{\mathbf{j}} \right. \\ &\left. - \frac{\partial p}{\partial y} + \frac{\partial}{\partial y}\left(2\mu \frac{\partial v}{\partial y}\right) + \frac{\partial}{\partial x}\mu\left(\frac{\partial v}{\partial x} + \frac{\partial u}{\partial y}\right) + \frac{\partial}{\partial z}\mu\left(\frac{\partial v}{\partial z} + \frac{\partial w}{\partial y}\right) + \Delta\rho g_y\right] \end{aligned} \tag{2.20}$$

$$\frac{\partial w}{\partial t}+\frac{\partial wu}{\partial x}+\frac{\partial wv}{\partial y}+\frac{\partial w^2}{\partial z}-w\left(\frac{1}{\rho_g}-\frac{1}{\rho_l}\right)\dot{m}_f=\frac{1}{\rho}\Bigg[\int_A \sigma_f\,\kappa\,\hat{\mathbf{n}}\,\delta(\mathbf{x}-\mathbf{x}_f)\,\mathrm{d}A_f\cdot\hat{\mathbf{k}}$$
$$-\frac{\partial p}{\partial z}+\frac{\partial}{\partial z}\left(2\mu\frac{\partial w}{\partial z}\right)+\frac{\partial}{\partial x}\mu\left(\frac{\partial w}{\partial x}+\frac{\partial u}{\partial z}\right)+\frac{\partial}{\partial y}\mu\left(\frac{\partial w}{\partial y}+\frac{\partial v}{\partial z}\right)+\Delta\rho g_z\Bigg] \quad (2.21)$$

The Marangoni effects are not regarded in the present numerical method, though can readily be included [Nas et al. (2006)].

2.2.3 Conservation of energy

The energy conservation in the incompressible flow with phase change (considered as a heat source or sink at the interface between phases) is given by

$$\frac{\mathrm{D}T}{\mathrm{D}t}=\frac{\partial T}{\partial t}+\mathbf{u}\cdot\nabla T=$$
$$\frac{1}{\rho c_p}\left\{\nabla\cdot k\nabla T-\left[1-(c_{p,g}-c_{p,l})\frac{T_{sat}}{h_{lg}}\right]\int_A\delta(\mathbf{x}-\mathbf{x}_f)\,\dot{q}_f\,\mathrm{d}A_f\right\} \quad (2.22)$$

The term in square brackets before the integral $\Lambda=1-(c_{p,g}-c_{p,l})\dfrac{T_{sat}}{h_{lg}}$ is a constant coefficient that accounts for the latent heat of vaporization due to different specific heats in the two-phase domain.

For 3D configuration, the energy equation is written with velocity components in 3 directions in convective form as given in Eq.2.23.

$$\frac{\partial T}{\partial t}+u\frac{\partial T}{\partial x}+v\frac{\partial T}{\partial y}+w\frac{\partial T}{\partial z}=$$
$$\frac{1}{\rho\,c_p}\left[\frac{\partial}{\partial x}\left(k\,\frac{\partial T}{\partial x}\right)+\frac{\partial}{\partial y}\left(k\,\frac{\partial T}{\partial y}\right)+\frac{\partial}{\partial z}\left(k\,\frac{\partial T}{\partial z}\right)-\Lambda\int_A\delta(\mathbf{x}-\mathbf{x}_f)\,\dot{q}_f\,\mathrm{d}A_f\right] \quad (2.23)$$

2.2.4 Consideration of interface

The mass-flux rate can be expressed in terms of a heat-flux rate through the interface as

$$\dot{m}_f=\frac{\dot{q}_f}{h_{lg}} \quad (2.24)$$

where the heat-flux rate, in turn, is defined in terms of temperature gradients in normal directions from the interface:

$$\dot{q}_f = k_g \left.\frac{\partial T}{\partial n}\right|_g^f - k_l \left.\frac{\partial T}{\partial n}\right|_l^f \ . \tag{2.25}$$

The interface motion in the normal direction due to phase change is described by

$$\frac{\mathrm{d}\mathbf{x}_f}{\mathrm{d}t} = [u_n\,\hat{\mathbf{n}}]_f \ , \tag{2.26}$$

where the normal velocity consists of the local field velocity and the phase-change velocity as follows:

$$u_n = \frac{1}{2}(\mathbf{u}_l + \mathbf{u}_g)\cdot\hat{\mathbf{n}} - \frac{\dot{m}_f}{2}\left(\frac{1}{\rho_g} + \frac{1}{\rho_l}\right) \ . \tag{2.27}$$

2.3 Non-dimensional parametrization

The essential non-dimensional parameters for simulations are density and viscosity ratios:

$$\gamma = \frac{\rho_l}{\rho_g}\,, \qquad \zeta = \frac{\mu_l}{\mu_g} \ . \tag{2.28}$$

The Prandtl number that relates momentum diffusivity to thermal diffusivity:

$$\mathrm{Pr} = \frac{\mu c_p}{k} \ . \tag{2.29}$$

The Stefan number that relates sensible heat to latent heat:

$$\mathrm{St} = \frac{c_{p,g}(T_\infty - T_{sat})}{h_{lg}} \ . \tag{2.30}$$

The Bond number that relates gravitational forces to capillary forces:

$$\mathrm{Bo} = \frac{d^2(\rho_g)g}{\sigma} \ . \tag{2.31}$$

The Archimedes number that relates gravitational forces to viscous forces:

$$\mathrm{Ar} = \frac{\rho\sqrt{g\,d^3}}{\mu^2}\ . \tag{2.32}$$

The Stokes number that relates the characteristic time of a droplet to a characteristic time of the flow:

$$\mathrm{Stk} = \frac{\rho_l U d}{2\mu_g}\ . \tag{2.33}$$

Next, the numerical method applied to the mathematical model is described.

Chapter 3

NUMERICAL METHOD AND ITS IMPLEMENTATION

3.1 Discretization

In the present front-tracking/finite-difference method, two types of three-dimensional grids operate in parallel for the flow domain and the interface as depicted in Fig.3.1.

A fixed, uniform, staggered marker-and-cell (MAC) Eulerian grid, as illustrated in Fig.3.3, is used to compute the set of governing equations (Eq.2.19-2.22) for momentum and energy fields of the flow domain. All scalar variables, encompassing material properties, pressure, and temperature, are strategically stored at the central point of an Eulerian grid cell. Concurrently, the vector components of the velocity find their storage locations at the centers of the faces of the Eulerian grid cell, as vividly illustrated in Fig.3.3. This spatial arrangement ensures an organized distribution of crucial parameters within the computational domain.

The interface, also called, the front, between phases is discretized using the Lagrangian grid constructed by explicitly tracked marker points that form triangular elements [Unverdi and Tryggvason (1992), Tryggvason et al. (2001), Tryggvason et al. (2011)] as shown in Fig.3.4. Due to the front motion described by Eq.2.26, the marker points and the elements need to be added or deleted to sustain a prescribed resolution of the front. This process is called front-restructuring and it is implemented using the 3rd-order Legendre polynomial fitting technique to keep the front curvature [Tryggvason et al. (2001)].

A 2D representation of two grids is illustrated in Fig.3.2 for a simpler and better understanding of the numerical method.

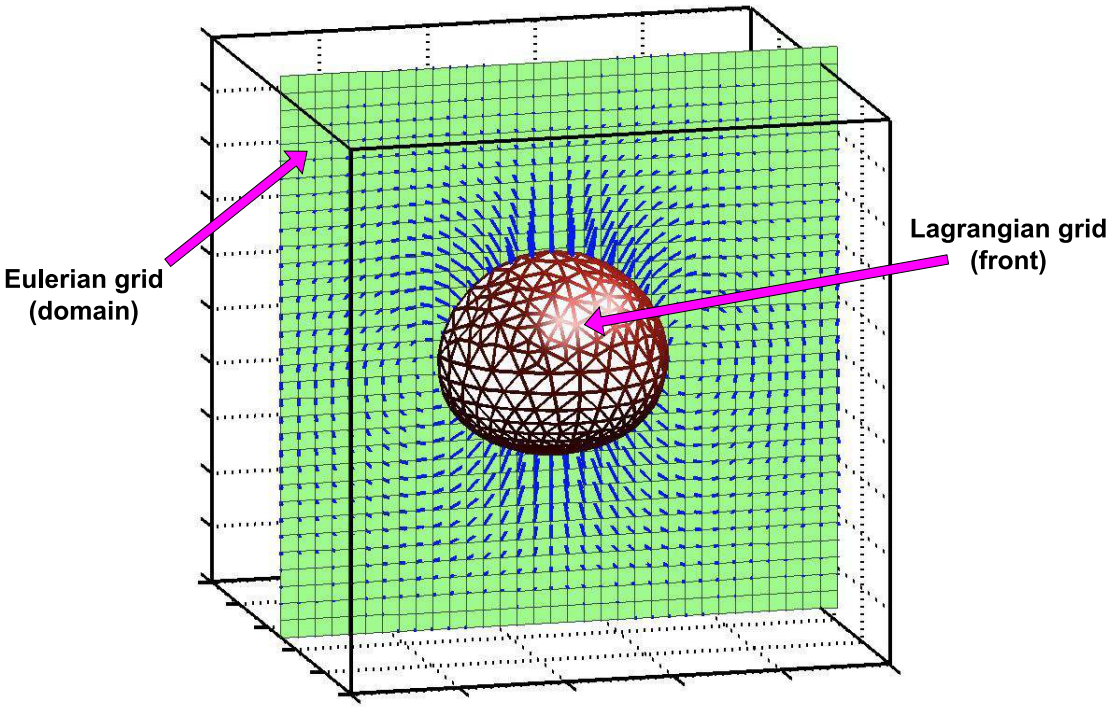

Figure 3.1: 3D representation of Eulerian and Lagrangian grids used in the present methodology.

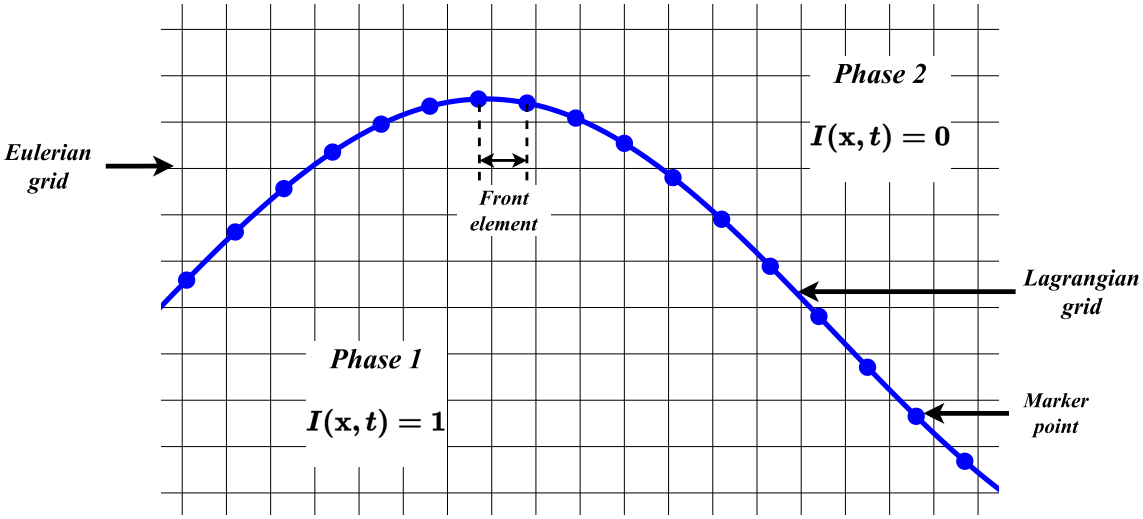

Figure 3.2: Representation of Eulerian and Lagrangian grids in 2D.

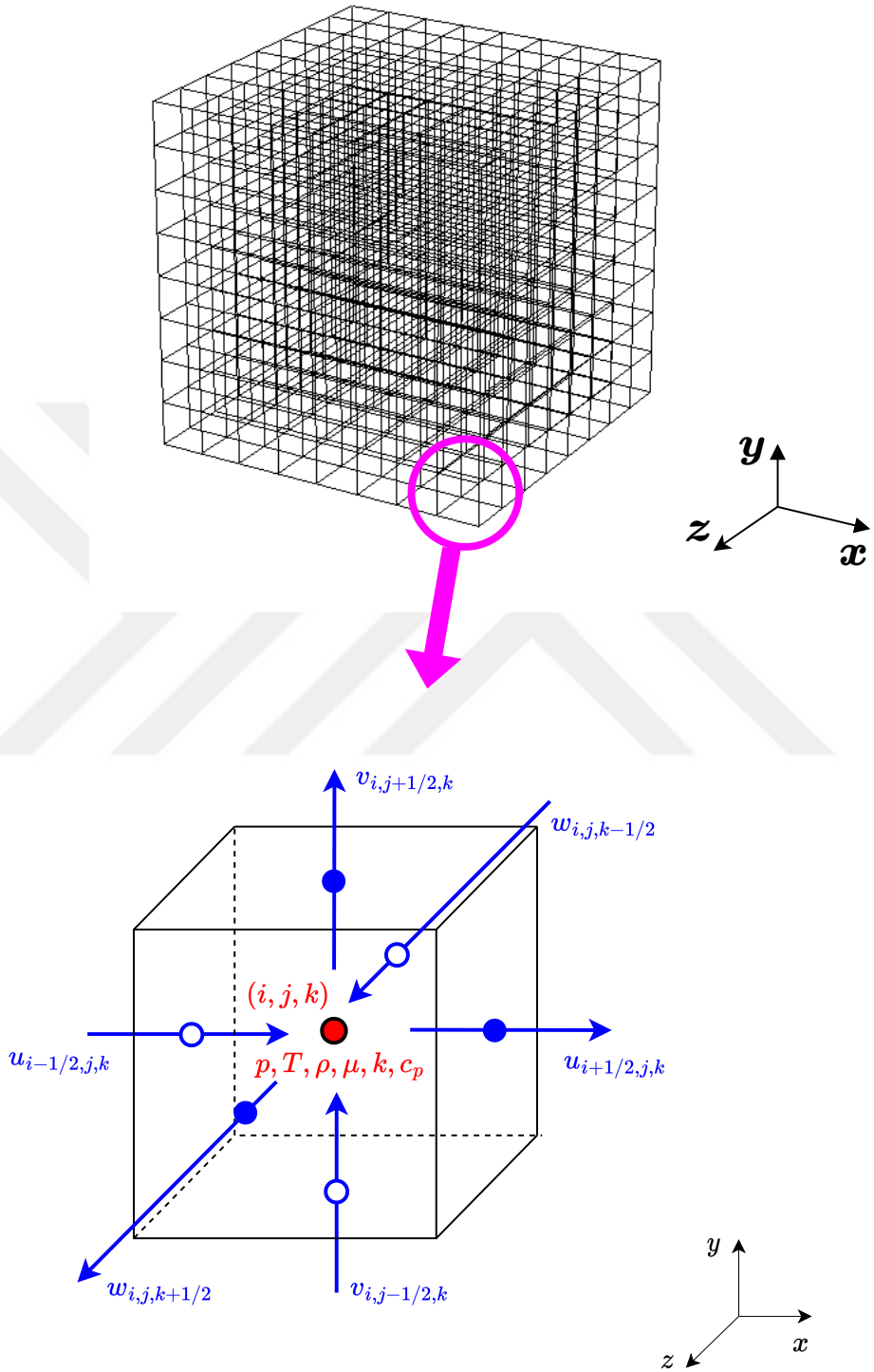

Figure 3.3: Representation of Eulerian grid for flow domain and staggered configuration for scalar and vector variables of an (i, j, k) cell in 3D.

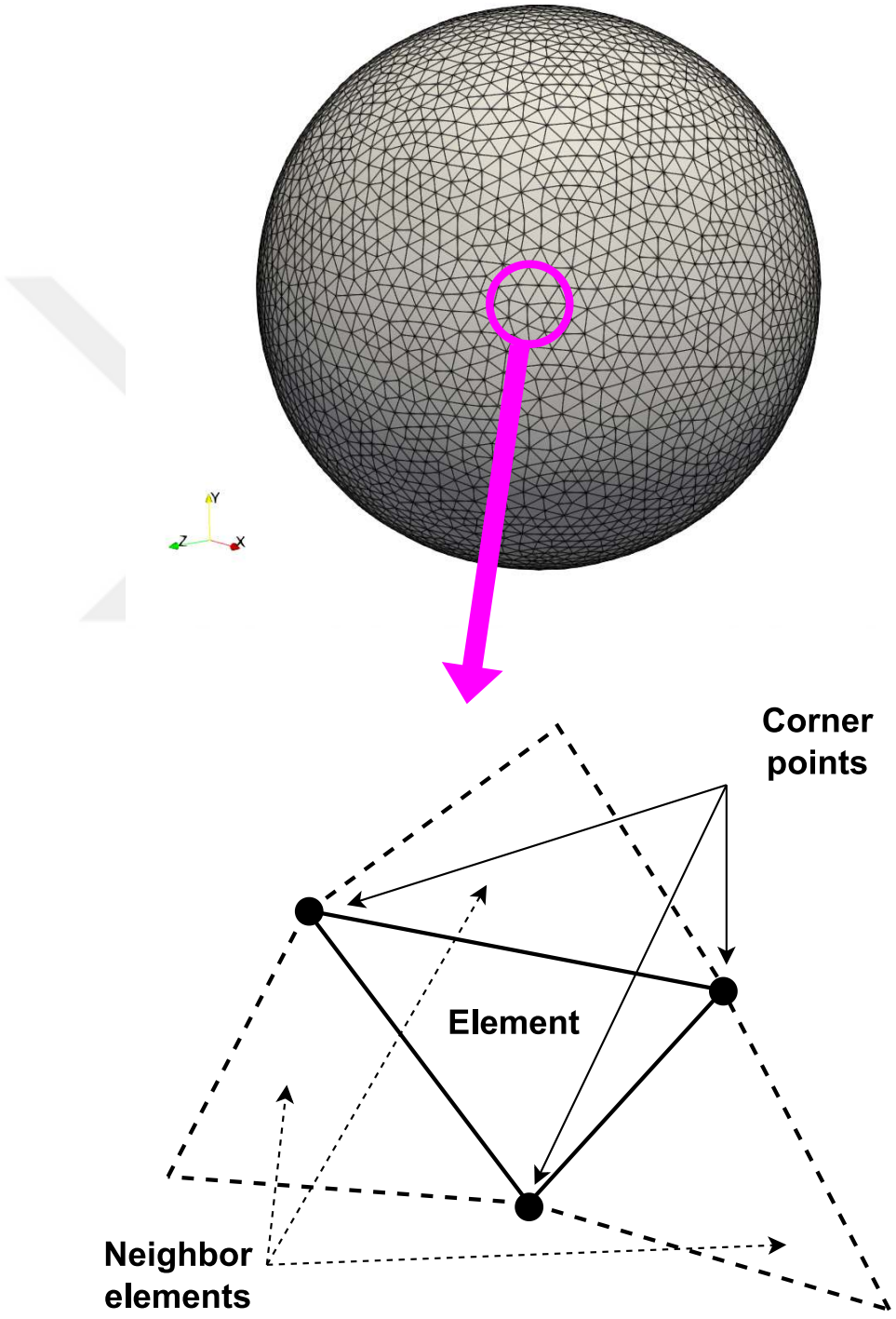

Figure 3.4: Representation of Lagrangian grid for the interface between phases and structure of its triangular elements made up by the marker points in 3D.

The solution is obtained in a coupled form using a front-tracking/finite-difference method, as described in works by Unverdi and Tryggvason (1992), Tryggvason et al. (2001), Juric and Tryggvason (1998), Esmaeeli and Tryggvason (2004), Tryggvason et al. (2011).

The discretization of the Navier-Stokes equations (2.19-2.21) involves a specific treatment on the right-hand side, where the pressure gradient term is separately accounted for, as expressed in Eq.3.1.

$$\frac{\mathbf{u}^{n+1} - \mathbf{u}^n}{\Delta t} = \mathbf{RHS}_M^n - \frac{1}{\rho^n} \nabla_h p \tag{3.1}$$

where the right-hand side is partitioned into specific terms for clearer categorization as shown in Eq.3.2.

$$\mathbf{RHS}_M^n = \underbrace{\mathbf{u}^n(\nabla_h \cdot \mathbf{u}^n) - \nabla_h \cdot \mathbf{u}^n\mathbf{u}^n}_{\text{advection term}} + \underbrace{\frac{\nabla_h \cdot \mu^n(\nabla_h \mathbf{u}^n + (\nabla_h \mathbf{u}^n)^T)}{\rho^n}}_{\text{diffusion term}} + \underbrace{\frac{\mathbf{f}_\sigma^n + \Delta\rho^n \mathbf{g}}{\rho^n}}_{\substack{\text{surface tension,} \\ \text{buoyancy, and} \\ \text{gravity terms}}} \tag{3.2}$$

The discretized momentum equation (Eq.3.1) can be solved employing a predictor-corrector method, specifically, the projection method outlined by Chorin (1968). During the prediction step, the algorithm deliberately omits the pressure gradient term and computes spatial derivatives of diffusive terms using second-order difference schemes as well as convective terms using the QUICK scheme [Leonard (1979)] to obtain a temporary or "predicted" velocity field. This initial estimation serves as a predictor for the subsequent correction step in the overall solution process.

$$\mathbf{u}^* = \mathbf{u}^n + \Delta t\, \mathbf{RHS}_M^n \tag{3.3}$$

In the correction step, it performs the vital task of "correcting" the unprojected velocity by including the pressure gradient term.

$$\mathbf{u}^{n+1} = \mathbf{u}^* - \frac{\Delta t}{\rho^n} \nabla_h p \tag{3.4}$$

For the pressure field, Eq.3.4 is rearranged and the divergence of both sides is taken to formulate a Poisson's equation (Eq.3.5) that is solved using the Fastest Fourier Transform in the West (FFTW) method for a 3D domain developed by Frigo and Johnson (2005).

$$\nabla_h^2 p = \frac{\rho^n}{\Delta t}(\nabla_h \cdot \mathbf{u}^* - \nabla_h \cdot \mathbf{u}^{n+1}) \tag{3.5}$$

where the divergence of the velocity field at the next time level is calculated using the discretization of Eq.2.17.

$$\nabla_h \cdot \mathbf{u}^{n+1} = \frac{1}{h_{lg}} \left(\frac{1}{\rho_g} - \frac{1}{\rho_l} \right) \left[\int_A \delta(\mathbf{x} - \mathbf{x}_f)\, \dot{q}_f \, \mathrm{d}A_f \right]^{n+1} \tag{3.6}$$

in which the heat flux at the front is discretized using the 1st-order one-sided finite-difference on Eq.4.1 [Esmaeeli and Tryggvason (2004), Udaykumar et al. (1996)].

$$\dot{q}_{f_m} = \frac{1}{\eta h} \left[k_g (T_{g_m} - T_{sat}) - k_l (T_{sat} - T_{l_m}) \right] \tag{3.7}$$

Temperature gradients are approximated using a length scale between values 1-2 with no significant effects on the solution [Esmaeeli and Tryggvason (2003), Esmaeeli and Tryggvason (2004), Al-Rawahi and Tryggvason (2004)] as demonstrated in Fig.3.5.

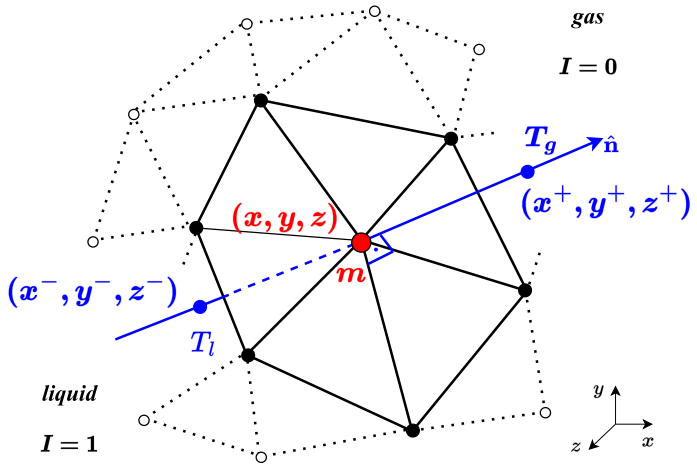

Figure 3.5: Illustration of temperature gradients approximation procedure.

The update of the temperature field over time is executed straightforwardly, as presented in Irfan and Muradoglu (2017).

$$T^{n+1} = T^n + \Delta t \, RHS_E^n \tag{3.8}$$

The computation of the right-hand side in Eq. 3.8 involves the incorporation of terms given in Eq.3.9.

$$RHS_E^n = - \underbrace{\mathbf{u}^n \cdot \nabla_h T^n}_{\text{advection term}} + \underbrace{\frac{\nabla_h \cdot k^n \nabla_h T^n}{\rho^n c_p^n}}_{\text{diffusion term}} - \underbrace{\frac{\Lambda}{\rho^n c_p^n} \left[\int_A \delta(\mathbf{x} - \mathbf{x}_f) \, \dot{q}_f \, \mathrm{d}A_f \right]^n}_{\text{heat source term}} \tag{3.9}$$

where the diffusion term is solved with the second-order difference scheme as in the momentum equation (3.2) while, for the advective term, the 5th-order WENO-Z scheme developed by Borges et al. (2008) is applied.

Every marker point on the front undergoes displacement through the discretization of Eq.2.26 with substituted Eq.2.27 as it is expressed in Eq.3.10.

$$\mathbf{x}_{f_m}^{n+1} = \mathbf{x}_{f_m}^n + \Delta t \left[\mathbf{u}_{f_m}^n - \frac{\dot{m}_{f_m}^n}{2} \left(\frac{1}{\rho_g} + \frac{1}{\rho_l} \right) \right] \tag{3.10}$$

After advancing the coordinates of the marker points, the indicator function is calculated in a manner analogous to the pressure field. This computation involves the utilization of the FFTW3 solver to solve Poisson's equation (Eq.3.11) [Tryggvason et al. (2001), Frigo and Johnson (2005)] obtained by taking the divergence of both sides in Eq.2.7:

$$\nabla_h^2 \, I^{n+1} = -\nabla_h \cdot \left[\int_A \hat{\mathbf{n}} \, \delta(\mathbf{x} - \mathbf{x}_f) \, \mathrm{d}A_f \right]^{n+1} \tag{3.11}$$

Afterward, the material properties in Eq.2.8-2.11 for the subsequent time level are computed using the updated indicator function.

The time integration, possessing second-order accuracy, is executed a timestep size that is determined by selecting the minimum value among the timesteps obtained from stability analyses of the convective, diffusive, and surface tension terms in the momentum and energy equations [Muradoglu and Tryggvason (2014), Irfan

and Muradoglu (2017)].

$$\Delta t = \min\left(\frac{h_{min}^2}{6\,\nu_{max}},\ \frac{h_{min}}{|\mathbf{u}|_{max}},\ \sqrt{\frac{(\rho_g+\rho_l)h_{min}^3}{4\pi\sigma}},\ \frac{h_{min}^2}{6\,\alpha_{max}}\right) \tag{3.12}$$

where $\nu = \dfrac{\mu}{\rho}$ and $\alpha = \dfrac{k}{\rho c_p}$ are the kinematic viscosity and the thermal diffusivity of fluids, respectively.

More detailed insights into the front-tracking method using the predictor-corrector scheme can be found in the works by Unverdi and Tryggvason (1992), Tryggvason et al. (2001) and Esmaeeli and Tryggvason (2004).

3.2 Distribution and interpolation

Communication of information between the stationary grid and the dynamic interface is essential throughout the solution process. To illustrate, parameters like surface tension, heat-flux, and mass-flux are initially computed at the interface. Subsequently, these values are smoothed onto the fixed Eulerian grid while solving the equations governing momentum and energy, respectively. Likewise, the velocity field is exclusively accessible at the fixed Eulerian grid nodes, necessitating interpolation onto the marker points in a conservative manner to accommodate the movement of the interface.

Following the methodology proposed by Tryggvason et al. (2001) and Tryggvason et al. (2011) when an interface quantity is smoothed onto a fixed grid node (i, j, k) or, otherwise, is averaged from the fixed grid nodes values in a three-dimensional domain, the following certain conditions must be satisfied:

$$\int_{\Delta A} \phi_f(x)\,\mathrm{d}A = \int_{\Delta V} \phi_{i,j,k}(\mathbf{x})\,\mathrm{d}V \tag{3.13}$$

Therefore, the discretized expression for interpolating Eulerian variables to Lagrangian ones is as follows:

$$\phi_f^m = \sum_i \sum_j \sum_k w_{i,j,k}^m\,\phi_{i,j,k} \tag{3.14}$$

and the discretized expression for distributing Lagrangian variables to Eulerian ones:

$$\phi_{i,j,k} = \sum_m \phi_f^m \, w_{i,j,k}^m \, \frac{\Delta A^m}{h^3} \tag{3.15}$$

The weights must adhere to the consistency condition to ensure the preservation of the total source strength when communicating from the interface to the grid and otherwise.

$$\sum_i \sum_j \sum_k w_{i,j,k}^m = 1 \tag{3.16}$$

The weight assigned to the grid node (i, j, k) for smoothing/averaging a quantity from the m-th marker point can be normalized as:

$$w_{i,j,k}^m = \frac{\tilde{w}_{i,j,k}^m}{\sum_i \sum_j \sum_k \tilde{w}_{i,j,k}^m} \tag{3.17}$$

where the non-normalized weights are derived as the product of one-dimensional distribution functions, namely:

$$\tilde{w}_{i,j,k} = d_C(x_f^m - ih) d_C(y_f^m - jh) d_C(z_f^m - kh) \tag{3.18}$$

here, (x_f^m, y_f^m, z_f^m) represent the coordinates of the m-th marker point, and the distribution function d_C is a slightly adapted form of Peskin's cosine function [Muradoglu and Tryggvason (2008), Muradoglu and Tryggvason (2014), Peskin (1977)], defined as:

$$d_C(r) = \begin{cases} \dfrac{1}{4h}\left(1 + \cos\dfrac{\pi\, r}{2h}\right) \text{ if } |r| < 2h \text{ and } \begin{cases} \text{if only liquid } I > 0.5 \\ \text{if only gas } I < 0.5 \end{cases} \\ 0 \quad \text{otherwise} \end{cases} \tag{3.19}$$

The one-sided interpolation method, illustrated in Fig. 3.6, is specifically employed to determine temperatures at gas and liquid phases, T_{g_m} and T_{l_m}, for Eq.3.7. In contrast, a two-sided distribution is applied to calculate the heat flux from the marker points to the fixed grid.

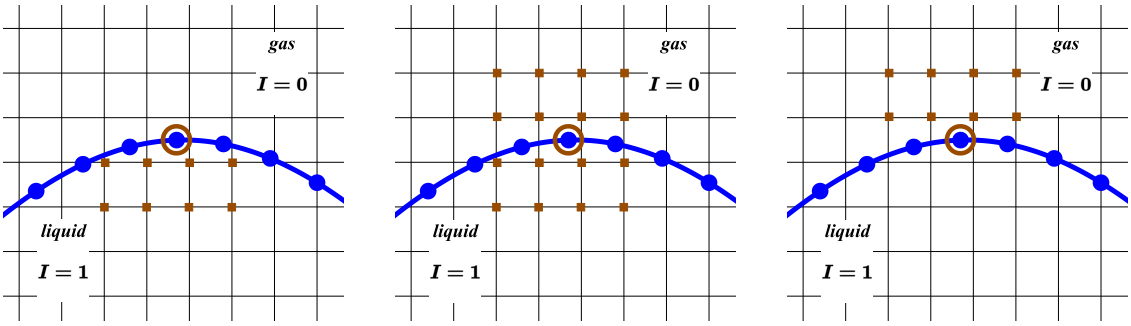

(a) One-sided in liquid phase. (b) Two-sided in both phases. (c) One-sided in gas phase.

Figure 3.6: Illustration of one-sided and two-sided distribution and interpolation procedures.

3.3 Parallelization

The numerical method is parallelized [Farooqi et al. (2019)] in a scalable way such that the domain with the Eulerian grid and the front with the Lagrangian are computed on separate processors. Though the domain is simulated on multiple processors while only one processor is used for the front, the latter can also be readily parallelized as the former.

The overall procedure after initialization is as follows:

1. Evaluate the timestep using Eq.3.12.
2. Store the old domain variables from the previous timestep.
3. Compute advection and diffusion of momentum in Eq.3.2.
4. Compute advection and diffusion of energy as well as for contribution of heat source in Eq.3.9.
5. Receive from the front processor to the domain processors the front data that are marker point coordinates, normal vectors, surface tension, and heatflux.
6. Advance front marker point coordinates using Eq.3.10 to the next timestep.
7. Send the advanced front marker point coordinates back to the front processor.
8. Compute the surface tension, buoyancy, and gravitational forces in Eq.3.2.

9. Calculate the predicted velocity using Eq.3.3 and update the temperature field using Eq.3.8.

10. Receive the advanced front data from the front processor.

11. Solve Poisson's equation for indicator function in Eq.3.11 based on the advanced front for the next timestep.

12. Compute the heat source with the advanced front data, the updated temperature field, and the newly solved indicator function using Eq.3.7 for the next timestep.

13. Send the advanced front heatflux back to the front processor.

14. Solve Poisson's equation for pressure in Eq.3.5.

15. Correct the velocity field using Eq.3.4 and update fluid properties using Eq.2.8-2.11 for the next timestep.

16. Repeat steps from 3 to 15 for the second-order time integration.

17. Average the domain variables with the stored old variables from 2 and start over from step 1 for the next iteration.

A flow chart of computation steps and data transfer in one timestep for parallel simulations is provided in Fig.3.7. Further information on parallelization and communication is available in the paper by Farooqi et al. (2019).

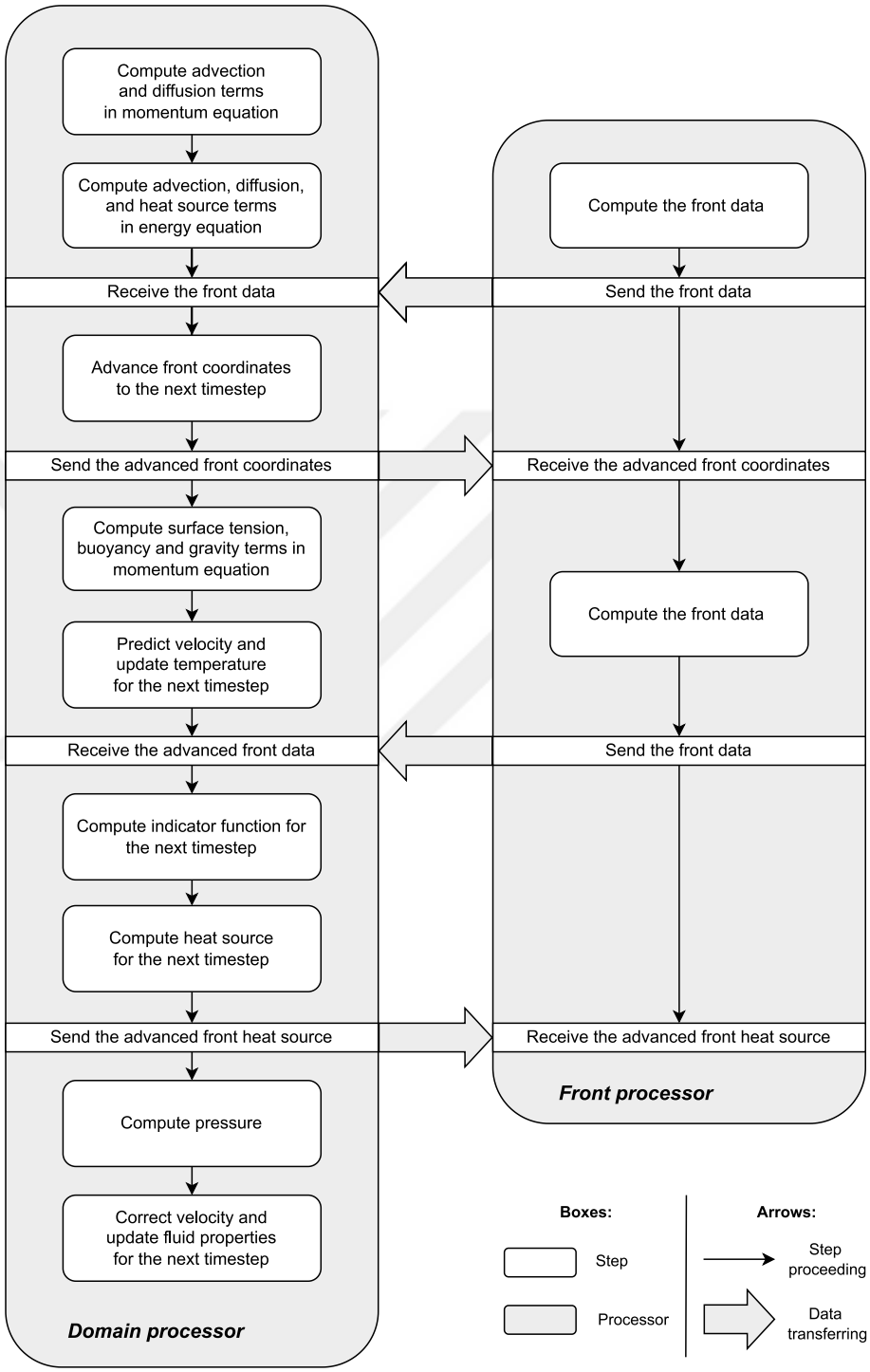

Figure 3.7: Flow chart of operations and communications during one timestep of a parallel simulation.

Chapter 4

RESULTS AND DISCUSSION

4.1 Validation 1: Heat conduction from a 3D static droplet

The numerical algorithm for solving the energy equation as well as for calculating and distributing the heat source needs to be tested similarly as in Muradoglu and Tryggvason (2008) and Muradoglu and Tryggvason (2014). For this purpose, a static spherical hot droplet of diameter $d = d_0$ is considered in an ambient bulk fluid as shown in Fig.4.1. It is positioned at the center of a cubic domain between two plates $(2.5d_0, 2.5d_0, 2.5d_0)$ with a side length of $L_x = L_y = L_z = 5d_0$. The temperature within the droplet is kept at $T_l = T_f = T_S = 2T_\infty$ such that a constant heat transfer occurs to the ambient environment that is initially two times colder ($T_g = T_\infty$) and it is supposed to stay cold at a distance far away from the droplet. In this configuration, the temperature field evolves by the one-dimensional heat equation given in Eq.4.1

$$\frac{\partial T}{\partial t} = \frac{\alpha}{r^2}\frac{\partial}{\partial r}\left(r^2\frac{\partial T}{\partial r}\right) \tag{4.1}$$

with the following initial and boundary conditions

$$\textbf{I.C. :} \begin{cases} T(r \leq R, t = 0) = T_S = 2T_\infty \\ T(r > R, t = 0) = T_\infty \end{cases} \tag{4.2}$$

$$\textbf{B.C. :} \begin{cases} T(r \leq R, t) = T_S = 2T_\infty \\ T(r \to \infty, t) = T_\infty \end{cases} \tag{4.3}$$

An approximate solution to Eq.4.1 is provided by Muradoglu and Tryggvason (2008) as

$$T(r,t) = T_\infty + \frac{R}{r}\left[1 - \text{erf}\left(\frac{r-R}{2\sqrt{\alpha\, t}}\right)\right](T_S - T_\infty) \tag{4.4}$$

Note that Eq.4.4 is not a correct analytical solution but it gives a good approximation as discussed by Muradoglu and Tryggvason (2014). Equation 4.1 also can be computed by the forward time-forward space finite-difference scheme

$$T_i^{n+1} = T_i^n + \frac{\alpha \Delta t}{4\Delta r^2}\left[\left(1+\frac{r_{i+1}}{r_i}\right)^2 (T_{i+1}^n - T_i^n) - \left(1+\frac{r_{i-1}}{r_i}\right)^2 (T_i^n - T_{i-1}^n)\right] \quad (4.5)$$

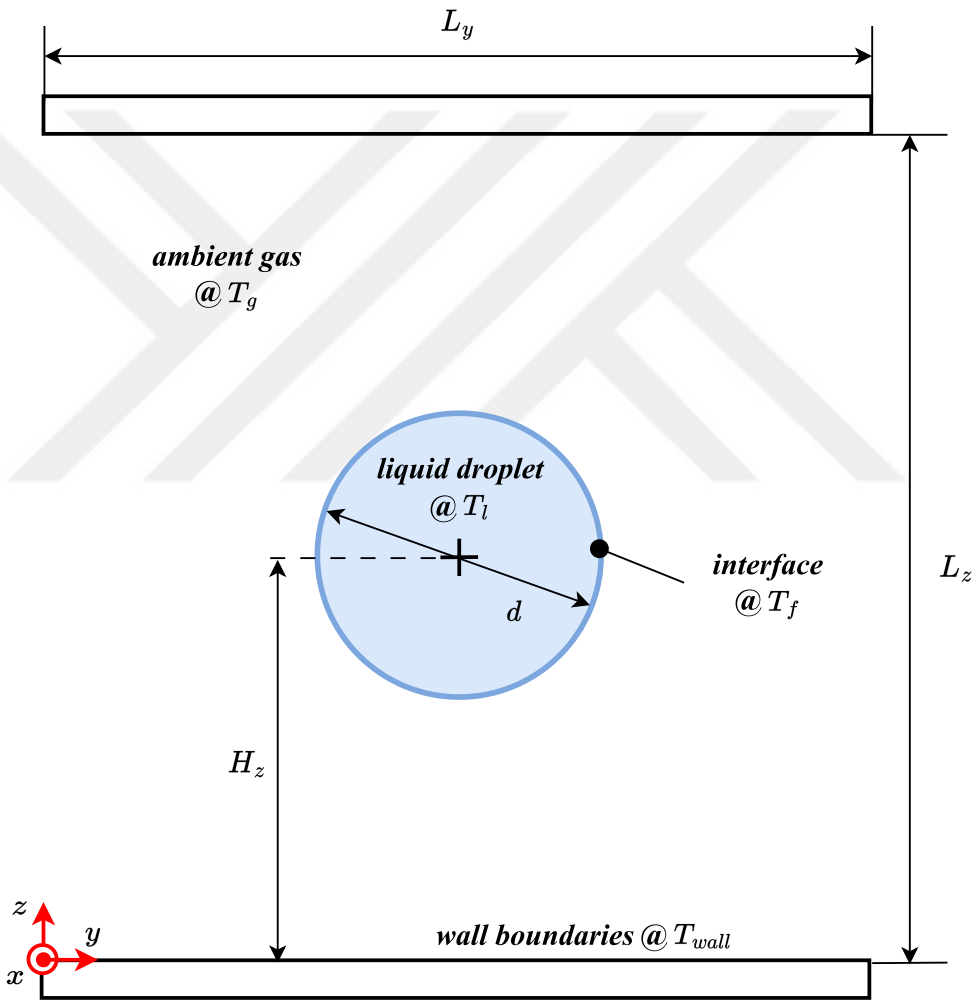

Figure 4.1: Schematic illustration of a 3D droplet with a diameter, d, positioned between two plates at $(0.5L_x, 0.5L_y, H_z)$, presented as a slice along the z-y plane within the cubic domain of size $L_z = L_y = L_x$ (out of the page). This slice is normal to the x-direction and it is cut at $x = 0.5$. The origin of the Cartesian coordinate axes is at the bottom left corner (red). T_g, T_l, T_f, T_{wall} represent temperatures of ambient gas, the droplet interior (light blue), the droplet interface (blue), and the upper and lower plates' wall boundaries (that can have different values), respectively.

The analytical solution of Eq.4.4 and the iterative solution of Eq.4.5 are compared with the results from a simulation with the computational domain discretized using the present method on a grid of dimensions $256 \times 256 \times 256$. The simulation configuration is $Pr_g = 0.32$ which relates kinematic terms to thermal terms as given in Eq.2.29. All corresponding variables are non-dimensionalized with the length scale $l^* = d/2$, the time scale $t^* = d^2/4\alpha_g$, and the temperature scale $T^* = T_\infty$.

The comparison of temperature profiles is depicted in Fig.4.2 at different time points from which a good alignment of the results is achieved that indicates accurate treatment of the heat exchange between phases and the temperature diffusion in the ambient phase.

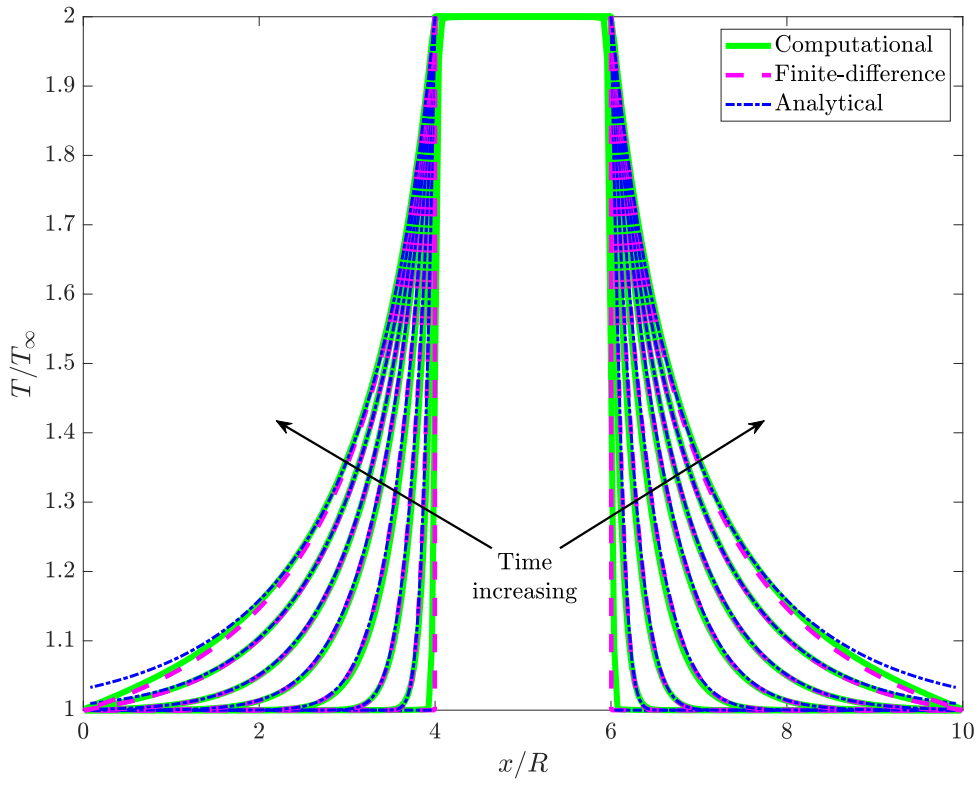

Figure 4.2: Comparison of temperature profiles from analytical, finite-difference, and computational results at various time points for validation of temperature diffusion and heat transfer from a 3D static droplet.

4.2 Validation 2: Evaporation of a 3D stationary droplet

In this test case, the simulation represents the evaporation of a stationary droplet within the 3D setup as in Validation 1 (Fig.4.1). A droplet with the initial diameter $d = d_0$ is positioned at the center of the domain ($L_x = L_y = L_z = 5d_0$) between two plates and its temperature is kept constant and equal to the front temperature regarded as saturated, i.e., $T_l = T_f = T_{sat} = 373\,\mathrm{K}$, through the course of the evaporation that is driven due to initially hotter ambient gas ($T_g = T_\infty > T_{sat}$). The Dirichlet boundary conditions are applied for temperature ($T_{wall} = T_\infty$) at the walls, and vapors are permitted to exit the domain freely. The non-dimensional parameters calculated using the physical properties are the density ratio $\gamma = 5.0$, the viscosity ratio $\zeta = 9.0$, the Prandtl number in liquid phase $\mathrm{Pr}_l = 59.1$, the Prandtl number in gas phase $\mathrm{Pr}_g = 0.32$, and the Stefan number that characterizes the evaporation of the droplet. It is adjusted by changing the initial temperature of the ambient gas (T_∞), precisely, for three cases $\mathrm{St} = 0.1$, $\mathrm{St} = 0.05$, and $\mathrm{St} = 0.025$. All parameters are non-dimensionalized with the length scale $l^* = d_0$ and the time scale $t^* = d_0^2/\alpha_g$.

The d^2-law for an evaporating constant temperature droplet is given as

$$\frac{\mathrm{d}d^2}{\mathrm{d}t} = -\frac{8k_g}{\rho_l c_{p,g}} \ln\left(1 + \mathrm{St}\right) \tag{4.6}$$

that is solved for the squared diameter as follows

$$d^2 = d_0^2 - \frac{8k_g\, t}{\rho_l c_{p,g}} \ln\left(1 + \mathrm{St}\right) \tag{4.7}$$

Figures 4.3-4.5 demonstrate the grid convergence as the grid is refined for simulations using three different Stefan numbers. The solutions approach the d^2-law curve as the number of Eulerian grid cells within the front increases. Normalized squared diameters computational results are plotted with the analytical ones versus normalized time for all Stefan numbers in Fig.4.6 until the droplet reaches 50% mass-reduction. Fig.4.7 confirms that the FFTW3 solver used for the indicator function and pressure

fields are operating accurately. Fig.4.8 depicts the Stefan flow that appears as the droplet evaporates. The d^2-law is successfully validated for a n-heptane droplet in a hot environment at different temperatures as it is done by Irfan and Muradoglu (2018) and compared with the experimental Nomura et al. (1996), numerical Zhang (2004), as well as analytical results.

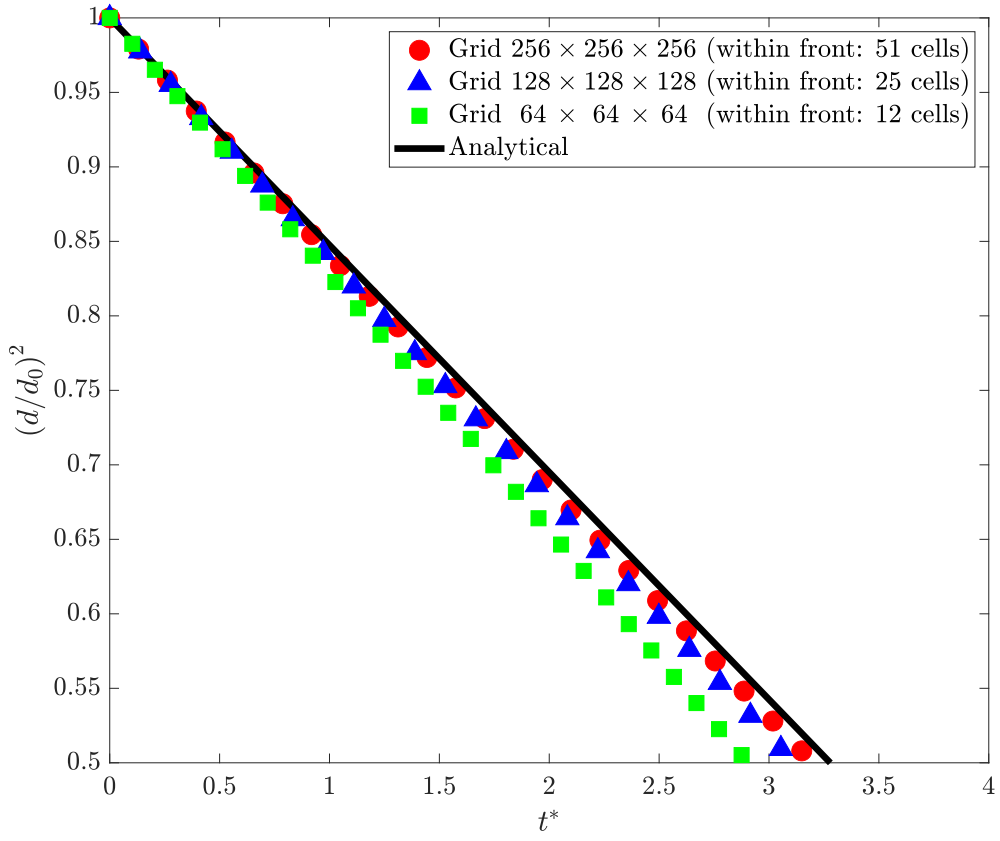

Figure 4.3: Grid convergence and validation with analytical d^2-law for $St = 0.1$. Normalized squared diameters on the y-axis are plotted versus normalized time on the x-axis. Grid: $256 \times 256 \times 256$.

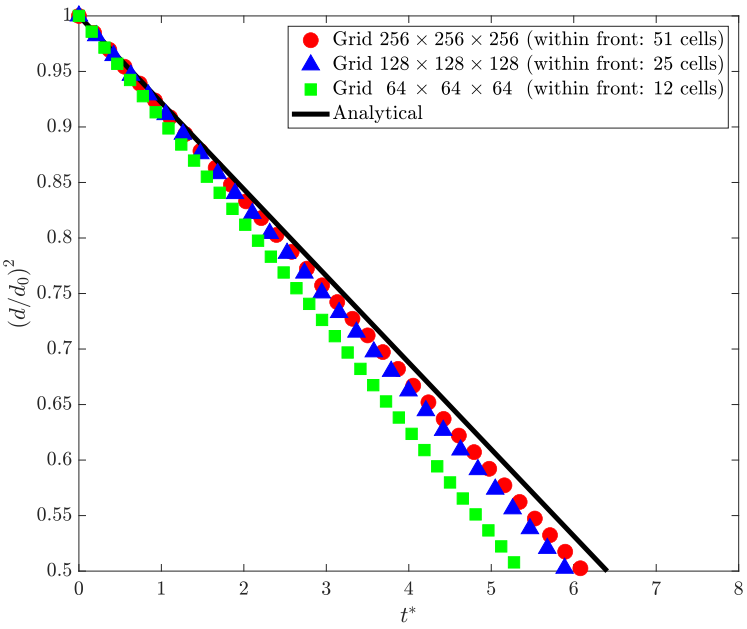

Figure 4.4: Grid convergence and validation with analytical d^2-law for $St = 0.05$. Grid: $256 \times 256 \times 256$.

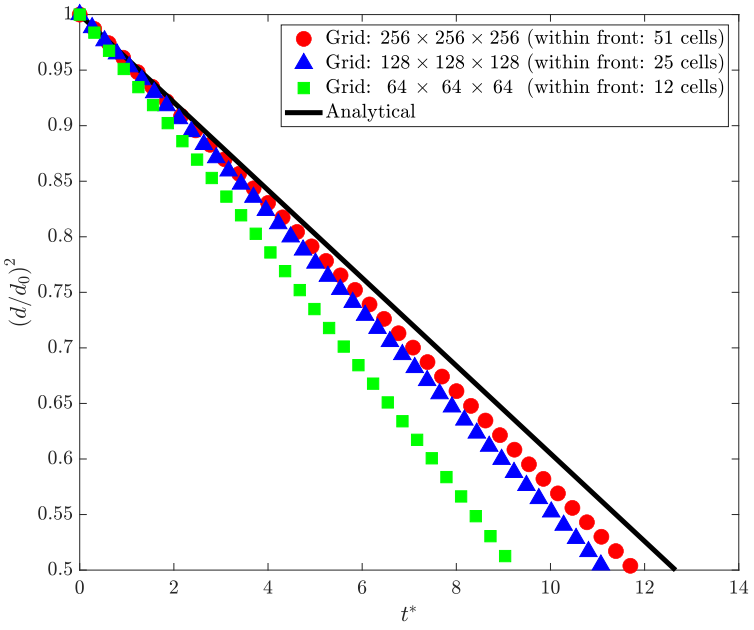

Figure 4.5: Grid convergence and validation with analytical d^2-law for $St = 0.025$. Grid: $256 \times 256 \times 256$.

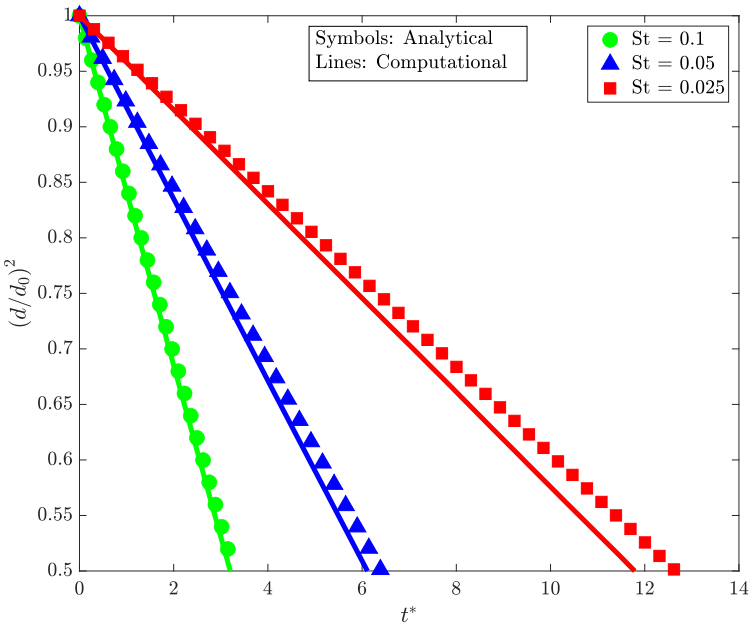

Figure 4.6: Comparison of computational results with the analytical d^2-law for various Stefan numbers. Grid: $256 \times 256 \times 256$.

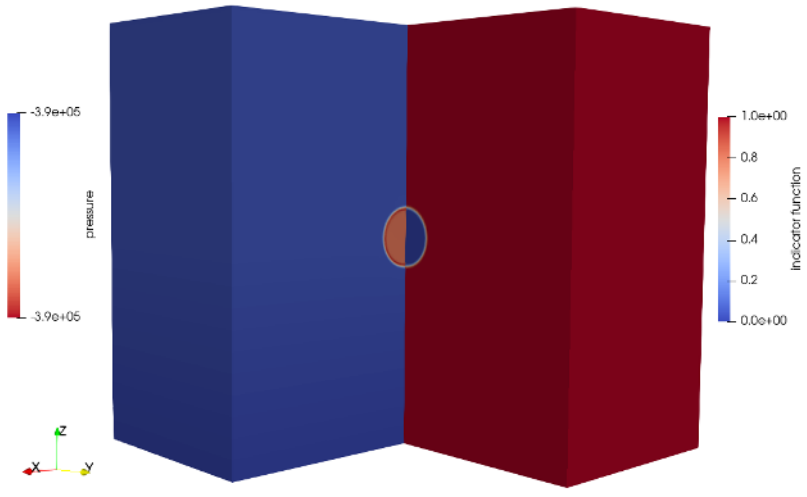

Figure 4.7: Pressure (left) and indicator function (right) fields for $St = 0.1$ at $t^* = 1.31$. Grid: $256 \times 256 \times 256$.

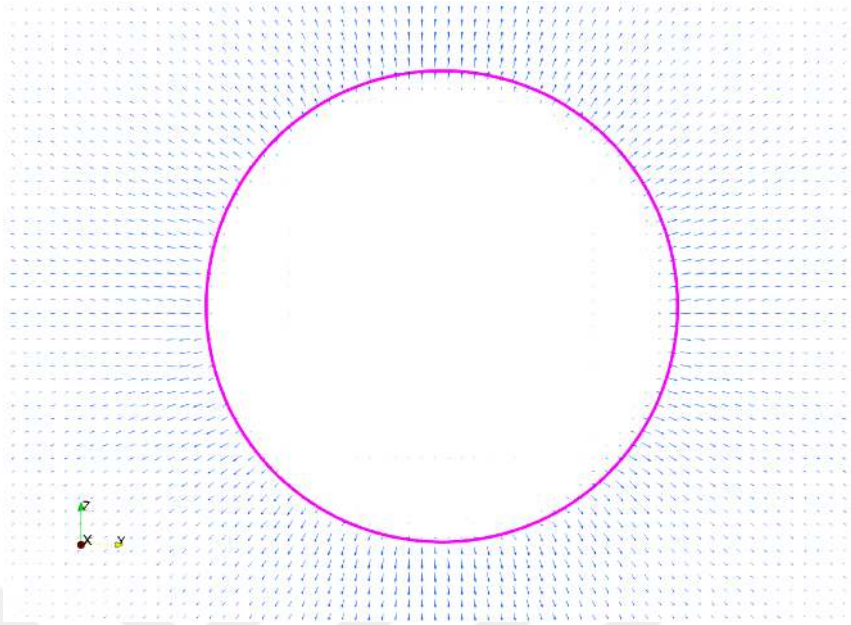

Figure 4.8: Velocity vector field in the vicinity of the evaporating droplet for $St = 0.1$ at $t^* = 1.31$. Grid: $256 \times 256 \times 256$.

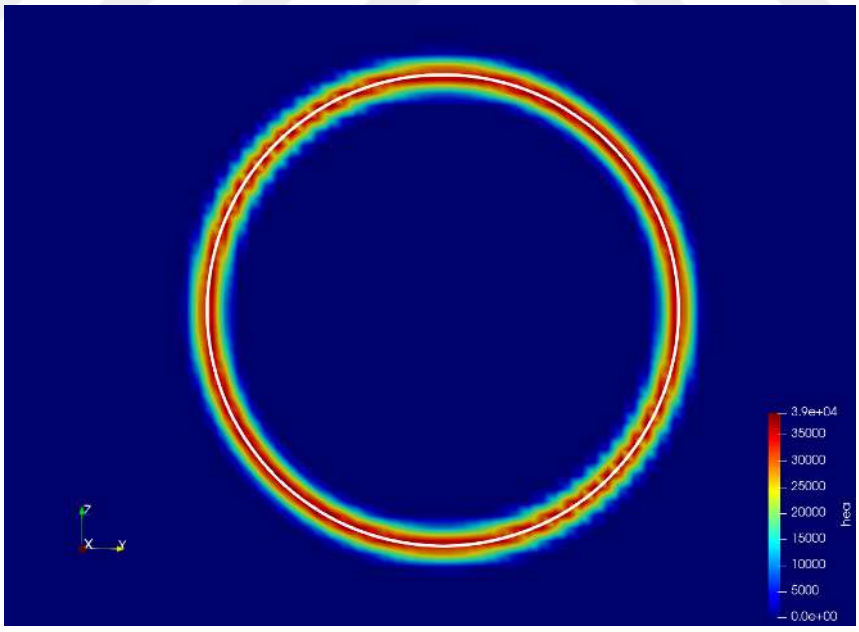

Figure 4.9: Heat distribution for $St = 0.1$ at $t^* = 1.31$. Grid: $256 \times 256 \times 256$.

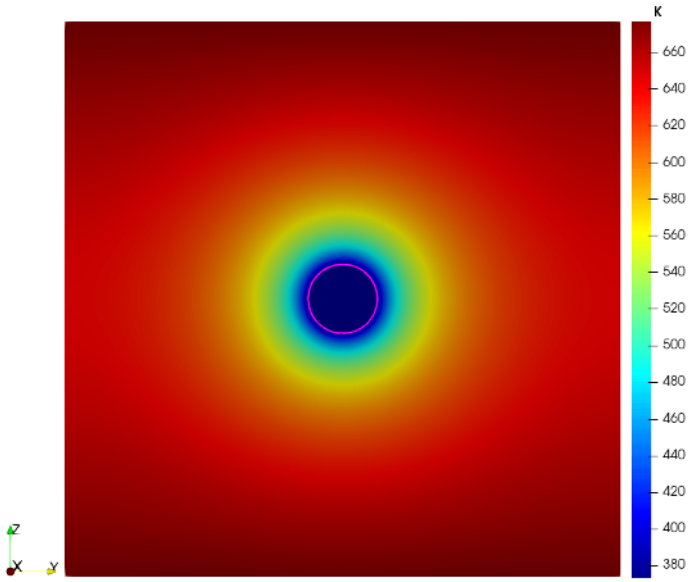

Figure 4.10: Temperature field for $St = 0.1$ at $t^* = 1.31$. Grid: $256 \times 256 \times 256$.

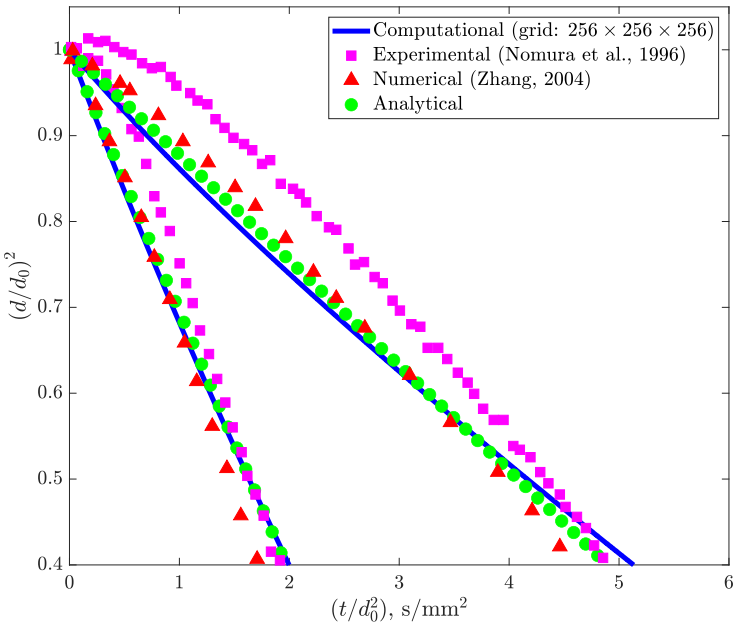

Figure 4.11: The d^2-law for n-heptane at two different temperatures compared with the experimental, numerical, and analytical results. Grid: $256 \times 256 \times 256$.

4.3 Validation 3: Evaporation of a 3D Leidenfrost droplet

To validate the method with the Leidenfrost phenomenon, a movable droplet within the 3D setup as illustrated in Fig.4.12 is simulated with a gravitational acceleration in the negative z-direction. The droplet with the initial diameter $d = d_0 = 2R$ is positioned at the center of the $x - y$ plane just above the hot lower plate $(2.5d_0, 2.5d_0, H_z = H_0)$ due to which evaporation is driven. Its temperature is kept constant and equal to the front temperature regarded as saturated i.e., $T_g = T_l = T_f = T_{sat}$. The Dirichlet boundary conditions are applied for the temperature at the hot lower plate $T_{wall,low} >> T_{sat}$, while at the upper plate, it is constant with the ambient gas $T_{wall,up} = T_{sat}$. Vapors are permitted to exit the domain freely. The non-dimensional parameters calculated using the physical properties are the Archimedes number of liquid phase $\mathrm{Ar}_l = 4.242$, the Prandtl number $\mathrm{Pr}_g = 0.71$ and the Stefan number in gas phase $\mathrm{St}_g = 0.12$, as well as the Bond number $\mathrm{Bo} = 0.08$ that characterize the Leidenfrost regime of the droplet. The Stokes number of in simulations is $\mathrm{Stk} = 68.7$.

The droplet center's z-coordinate is verified by grid convergence as it is seen in Fig.4.13. The minimum height from the hot wall to the droplet i.e., the lowest z-coordinate of the front is validated in Fig.4.14 with the expression for the minimum height from Eq.4.8 derived by Gordillo and Riboux (2022).

$$\frac{H_m}{R} = C_\tau \sqrt{\frac{8}{\pi}} \mathrm{Stk}^{-\frac{7}{6}} \left(\sqrt{1 + \frac{2}{3}\beta} - 1 \right)^{\frac{1}{2}} \tag{4.8}$$

where β is calculated using Eq.4.9 for the heated wall case.

$$\beta = \frac{\rho_l \, k_g (T_{wall} - T_{sat})}{\rho_g \, \mu_g h_{lg}} \tag{4.9}$$

Under acting gravity, the droplet gradually loses its sphericity while falling towards the hot wall, due to which, in turn, the cold ambient gas is being heated such that temperature rises in the positive z-direction with time evolution as it is depicted in Fig.4.15. Subsequently, temperature gradients across the droplet interface increase

generating the Stefan flow causing evaporation on the bottom surface of the droplet that is observed in Fig.4.16. The generated heat flux creates "a cushion" that allows flotation of the droplet above the hot wall with no impact on it as it is visualized in Fig.4.17, reaching the minimum height that with the value predicted by Gordillo and Riboux (2022) as it is seen in Fig.4.14.

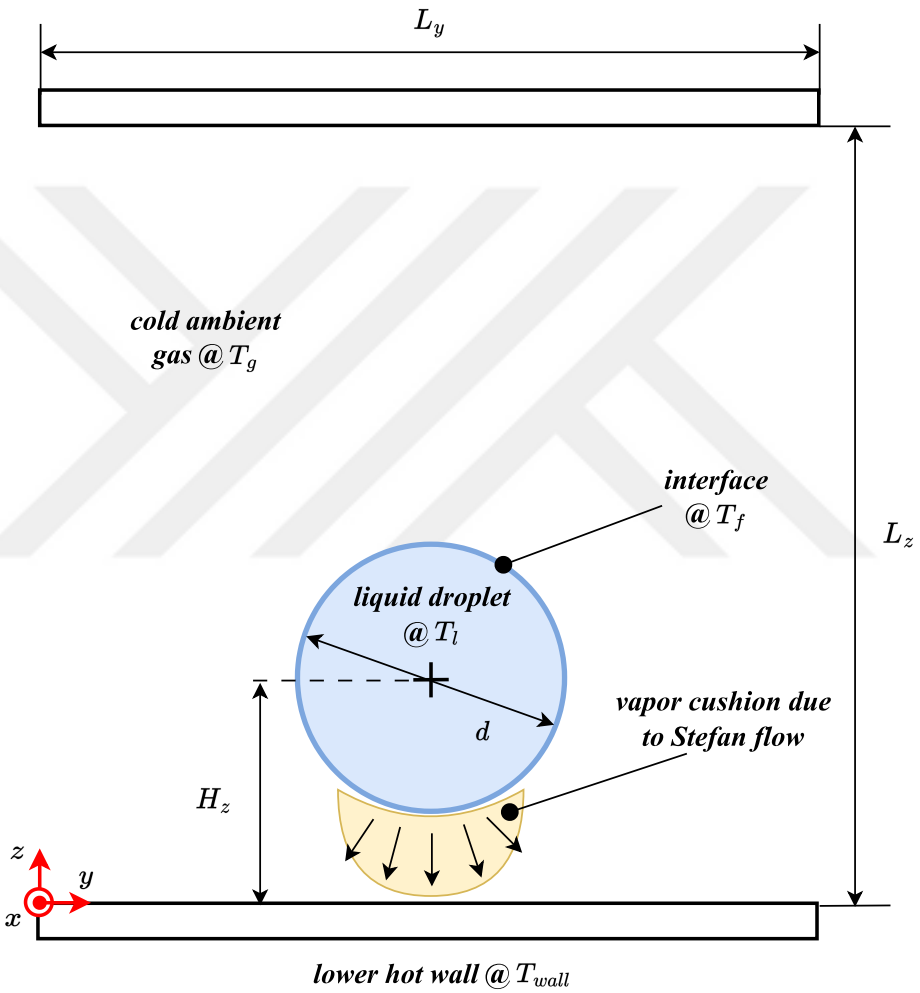

Figure 4.12: Schematic illustration of a 3D Leidenfrost droplet with a diameter, d, positioned between two plates at $(0.5L_x, 0.5L_y, H_z)$, presented as a slice along the z-y plane within the cubic domain of size $L_z = L_y = L_x$ (out of the page) such it is just above the lower hot plate. This slice is normal to the x-direction and it is cut at $x = 0.5$. The origin of the Cartesian coordinate axes is at the bottom left corner (red). T_g, T_l, T_f, T_{wall} represent temperatures of ambient gas, the droplet interior (light blue), the droplet interface (blue), and the lower hot plate wall boundaries, respectively. Stefan flow on the lower surface of the droplet creates a vapor cushion allowing the droplet flotation.

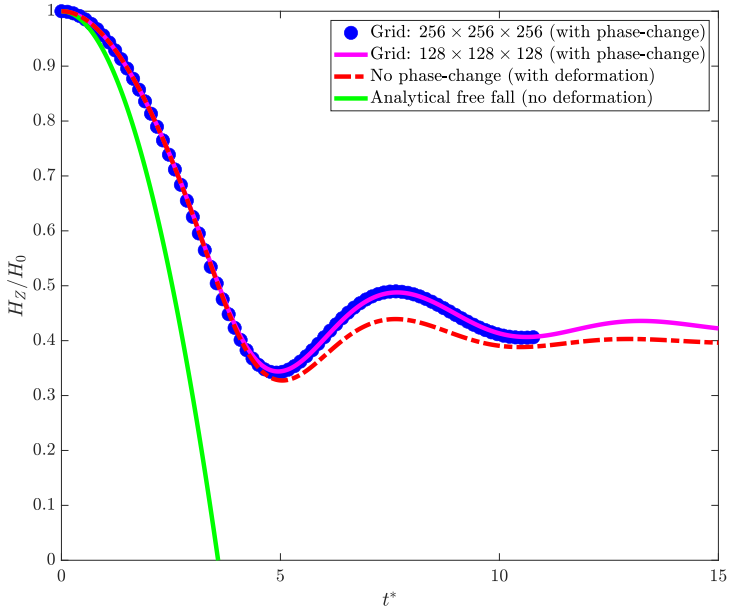

Figure 4.13: Grid convergence of the 3D Leidenfrost droplet center's z-coordinate at $Ar_l = 4.242$, $Pr_g = 0.71$, $St_g = 0.1$, and $Bo = 0.08$.

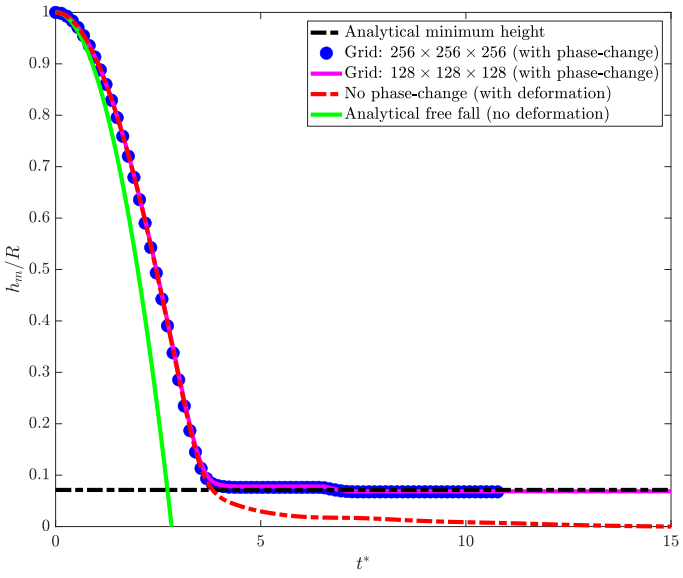

Figure 4.14: Comparison of the minimum z-coordinate of 3D Leidenfrost droplet for various cases with the analytical minimum height from Eq.4.8 derived by Gordillo and Riboux (2022) at $Ar_l = 4.242$, $Pr_g = 0.71$, $St_g = 0.1$, and $Bo = 0.08$.

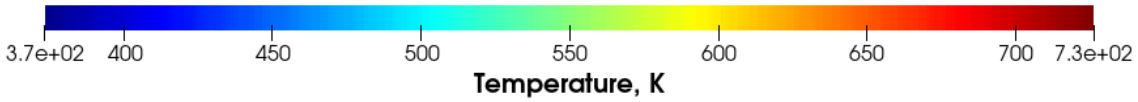

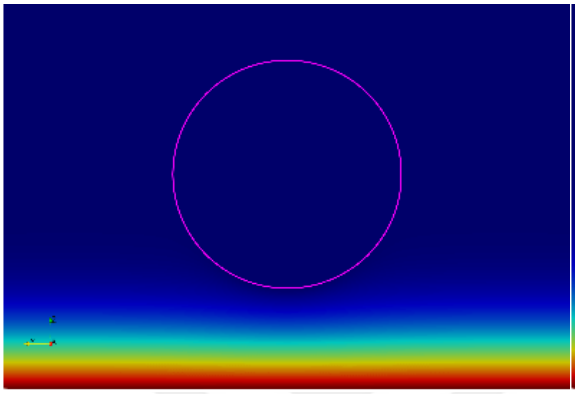

(a) $t^* = 1.09$

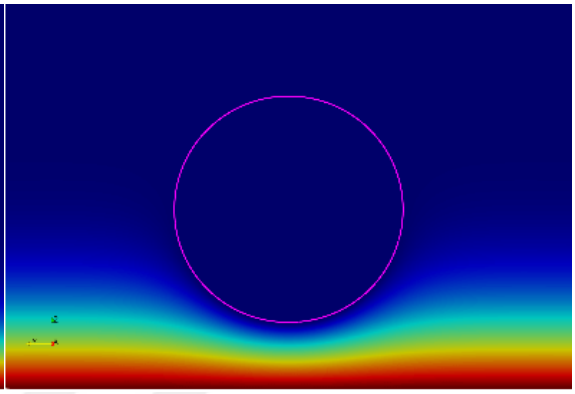

(b) $t^* = 2.18$

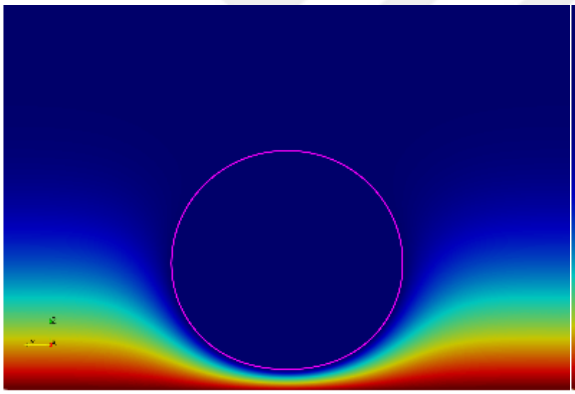

(c) $t^* = 3.27$

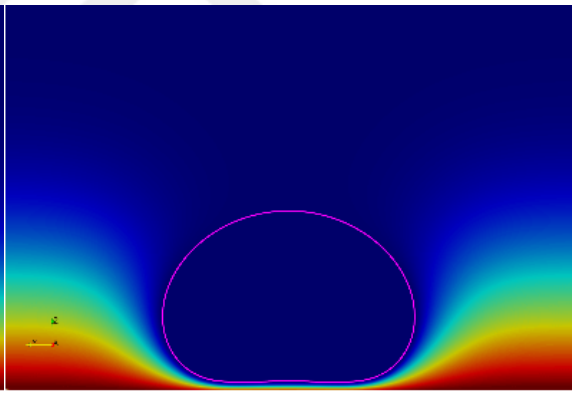

(d) $t^* = 4.36$

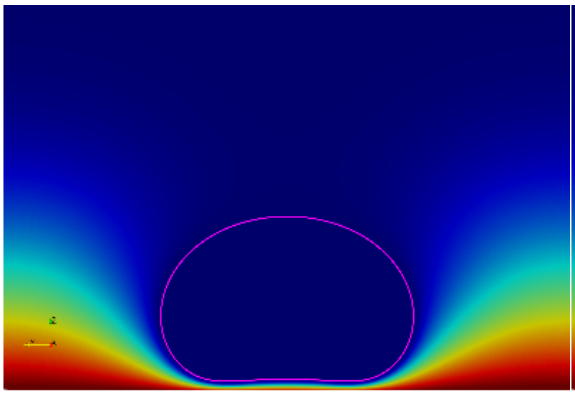

(e) $t^* = 5.45$

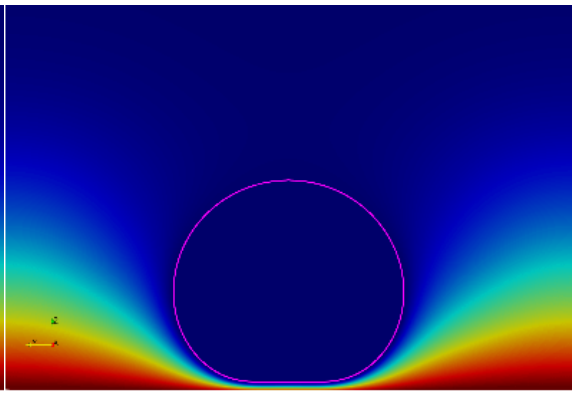

(f) $t^* = 6.55$

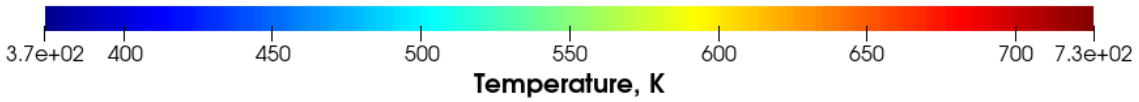

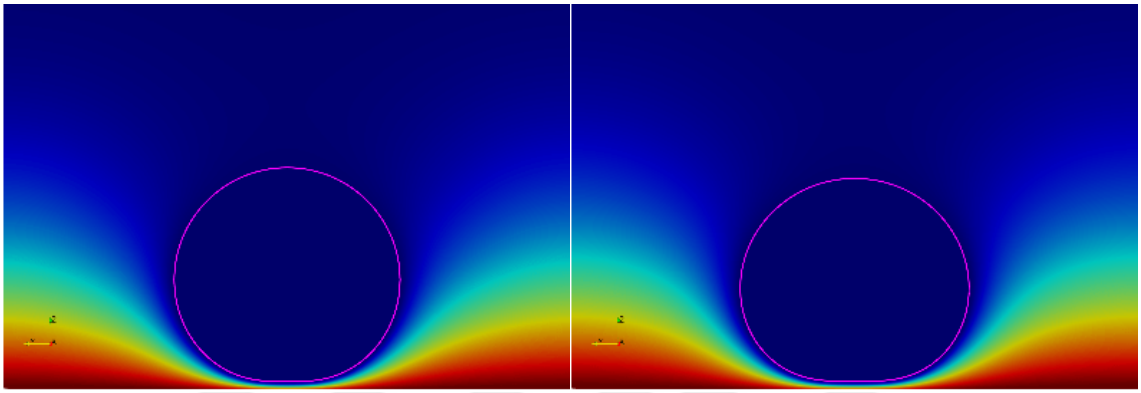

(g) $t^* = 7.64$ (h) $t^* = 8.73$

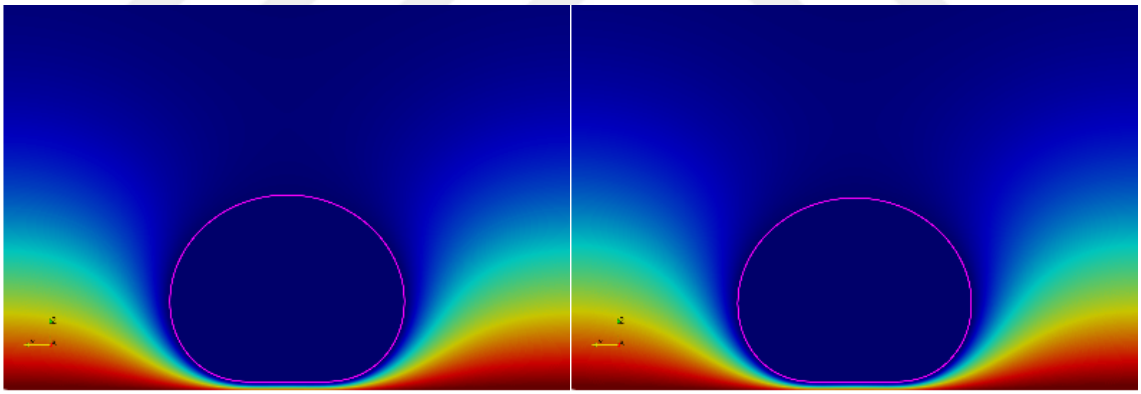

(i) $t^* = 9.82$ (j) $t^* = 10.91$

Figure 4.15: Evolution of temperature field in simulation of 3D Leidenfrost droplet evaporation with $Ar_l = 4.242$, $Pr_g = 0.71$, $St_g = 0.1$, and $Bo = 0.08$ at non-dimensional time levels. Grid: $256 \times 256 \times 256$.

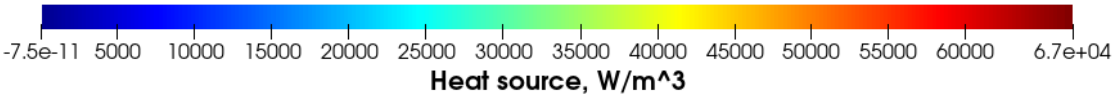

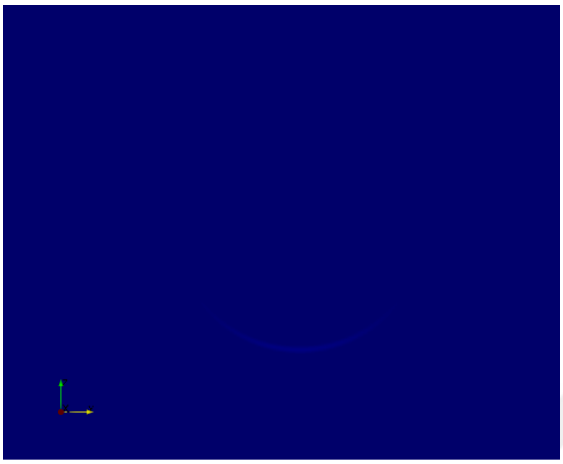

(a) $t^* = 1.09$

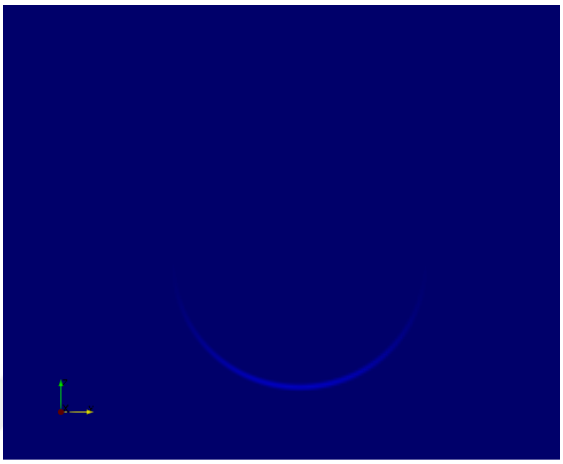

(b) $t^* = 2.18$

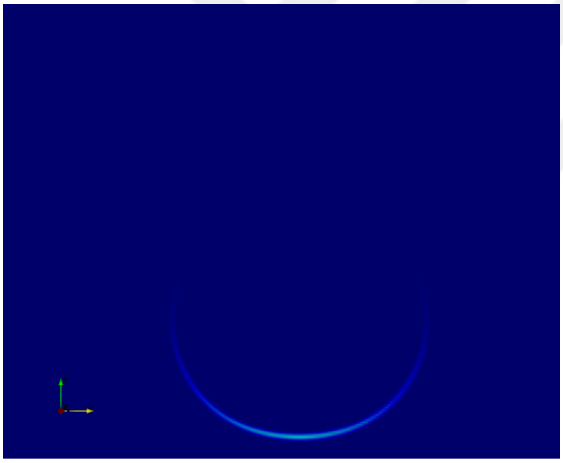

(c) $t^* = 3.27$

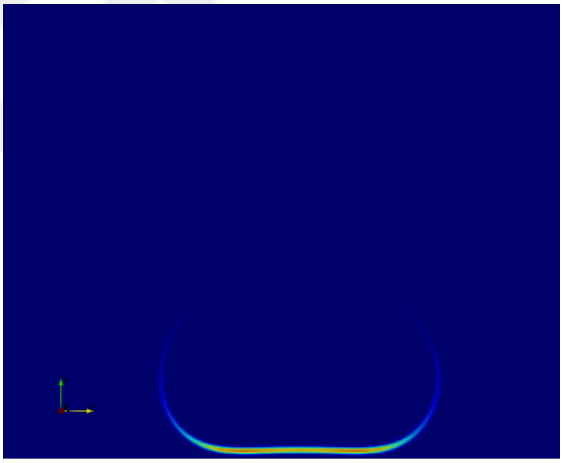

(d) $t^* = 4.36$

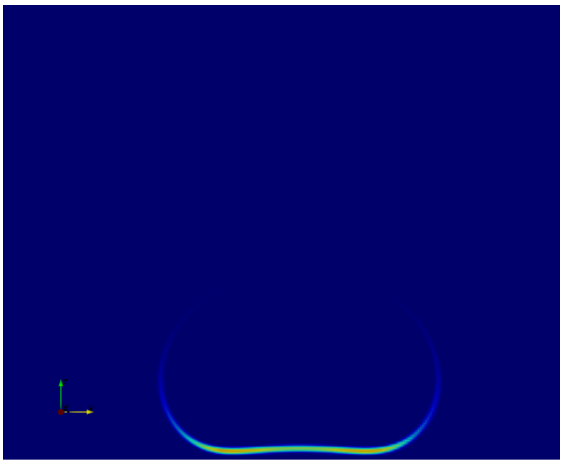

(e) $t^* = 5.45$

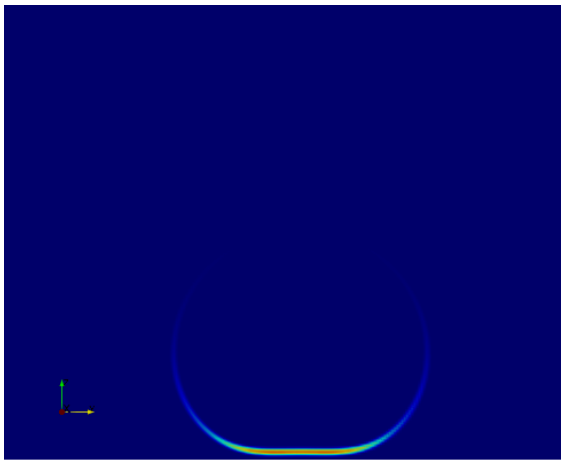

(f) $t^* = 6.55$

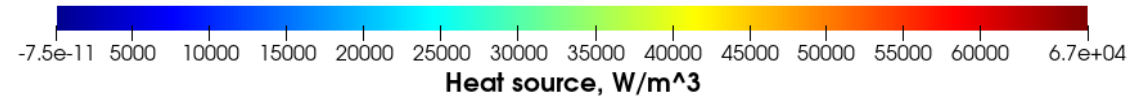

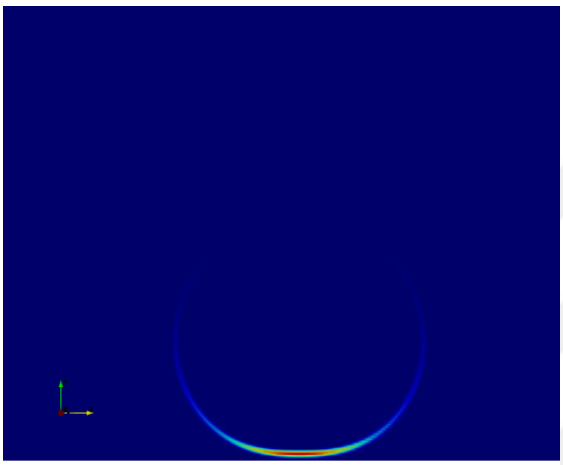

(g) $t^* = 7.64$

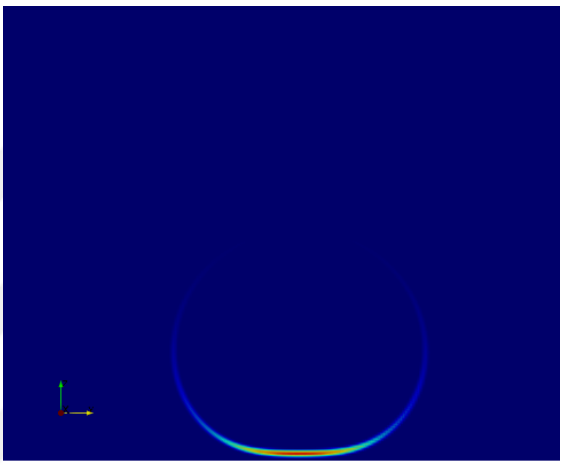

(h) $t^* = 8.73$

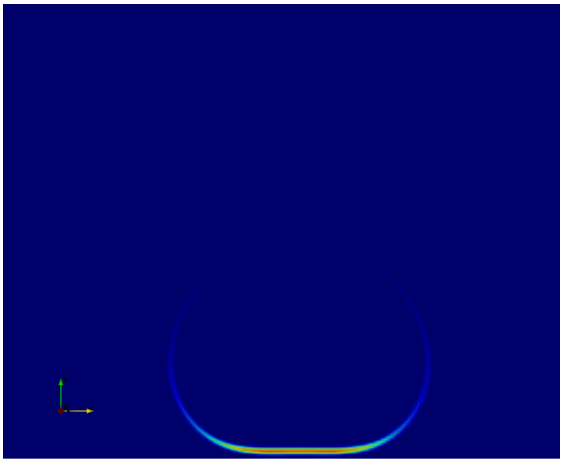

(i) $t^* = 9.82$

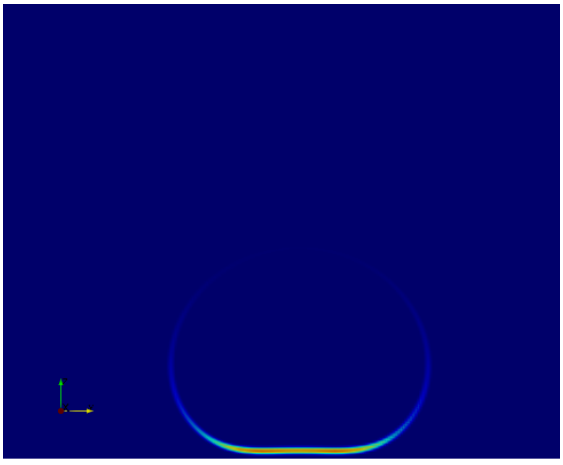

(j) $t^* = 10.91$

Figure 4.16: Evolution of evaporative heat field in simulation of 3D Leidenfrost droplet evaporation with $Ar_l = 4.242$, $Pr_g = 0.71$, $St_g = 0.1$, and $Bo = 0.08$ at non-dimensional time levels. Grid: $256 \times 256 \times 256$.

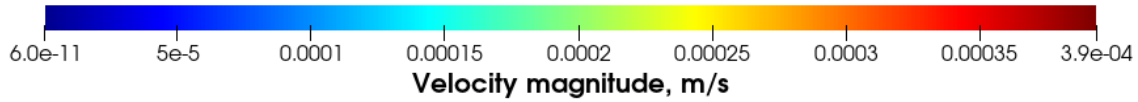

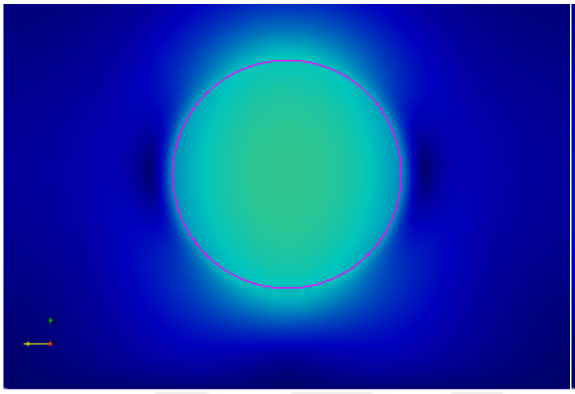

(a) $t^* = 1.09$

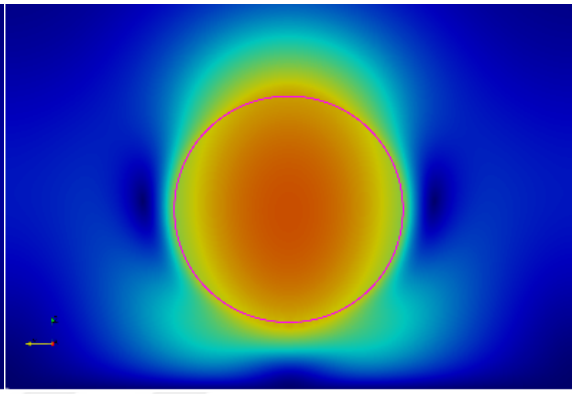

(b) $t^* = 2.18$

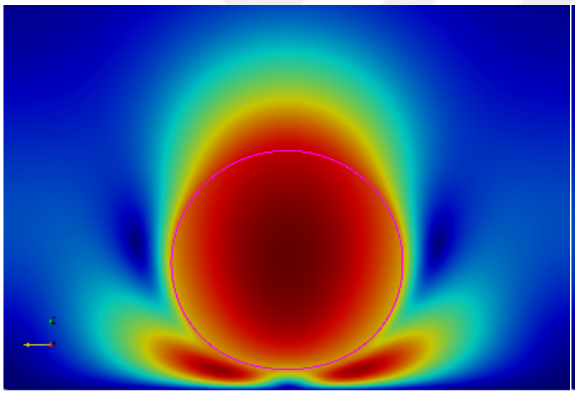

(c) $t^* = 3.27$

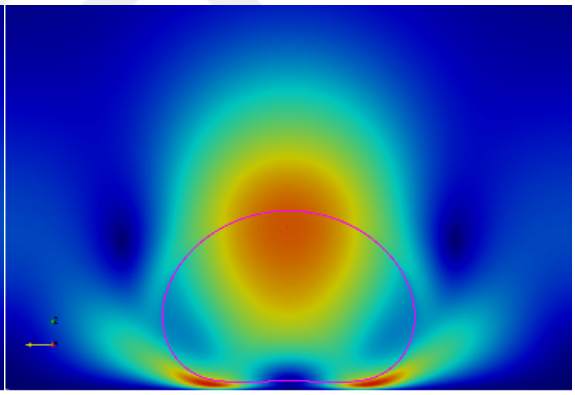

(d) $t^* = 4.36$

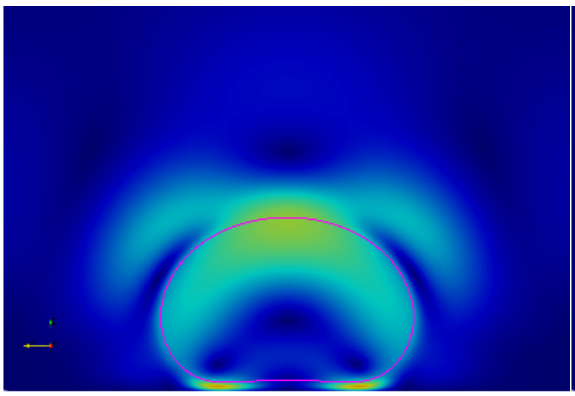

(e) $t^* = 5.45$

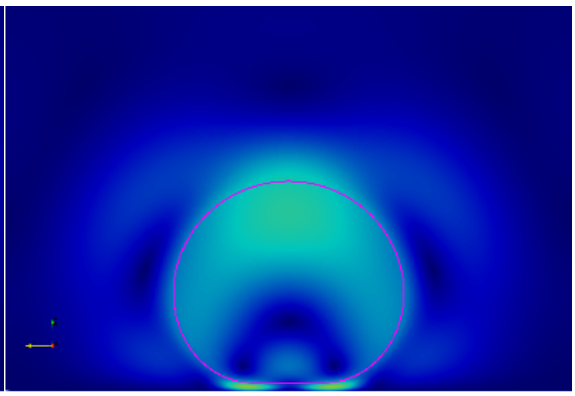

(f) $t^* = 6.55$

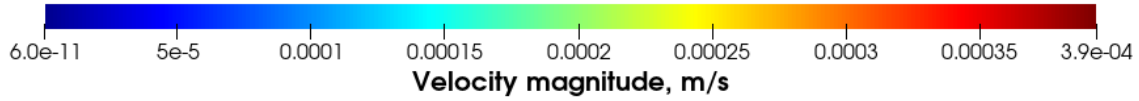

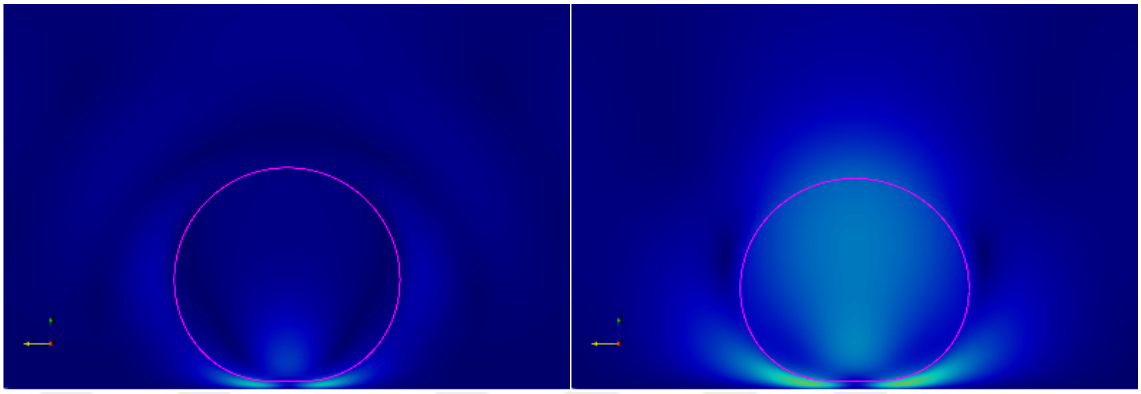

(g) $t^* = 7.64$ (h) $t^* = 8.73$

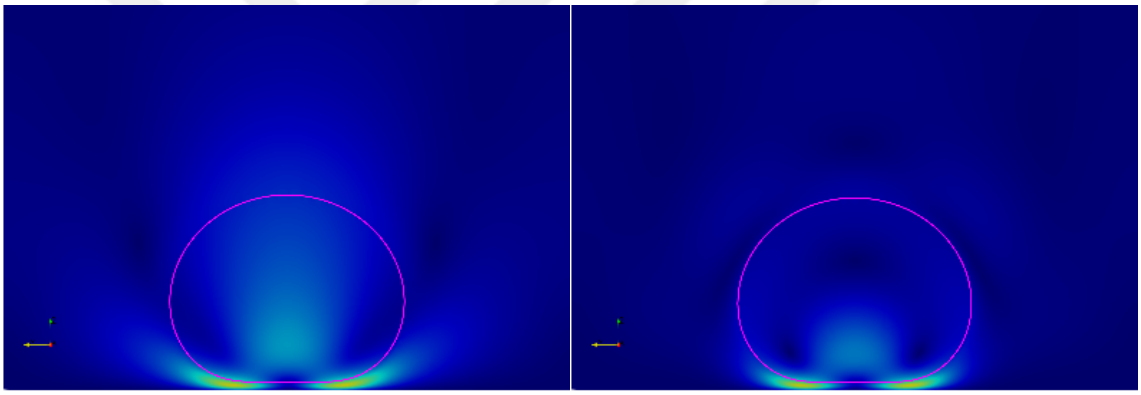

(i) $t^* = 9.82$ (j) $t^* = 10.91$

Figure 4.17: Evolution of velocity field in simulation of 3D Leidenfrost droplet evaporation with $Ar_l = 4.242$, $Pr_g = 0.71$, $St_g = 0.1$, and $Bo = 0.08$ at non-dimensional time levels. Grid: $256 \times 256 \times 256$.

The simulated droplet is observed in its Leidenfrost regime which is anticipated for the selected non-dimensional parameters following the work by Karami et al. (2017) except for the initial contact angle. It is set to 180^o instead of 60^o (no contact from $t = 0$)), therefore the droplet preserves its spherical shape longer than in the simulation by Karami et al. (2017).

Chapter 5

CONCLUSION

The culmination of this thesis lies in the enhancement of a numerical technique, specifically, a parallel front-tracking/finite-difference method tailored for multi-phase system simulations as developed by Tryggvason et al. (2011), Farooqi et al. (2019), Irfan and Muradoglu (2017). The conservation equations governing energy, incorporating a temperature gradient-driven phase change model are consistently coupled and computed. The finite-difference component of the method, employed for calculating scalar fields, is aptly utilized to evolve a scalar temperature field within a 3D-Cartesian, uniform, fixed, staggered Eulerian grid. Simultaneously, the front-tracking component dynamically resolves the interface, accounting for changes due to heat and mass transfer between phases, on a 3D unfixed and unstructured Lagrangian grid. Additional subroutines dedicated to temperature field evolution and droplet evaporation undergo successful verification through grid-convergence studies and effective validation against the heat equation and the theoretical d^2-law, respectively. Ultimately, the refined numerical method undergoes testing via the simulation of a 3D Leidenfrost droplet evaporation above a heated surface. This robust methodology equips us with the capability to simulate a diverse array of two-phase flows involving phase transitions in a 3D domain and its implementation can be readily integrated with techniques by Muradoglu and Tryggvason (2014) and Naseer et al. (2023) to study the effects of surfactants and viscoelasticity on phase transitions. The numerical method can also be extended to facilitate interaction between the droplet and wall boundaries, for this purpose, a contact line should be considered. Lastly, some parts of the method may be attempted to be computed using graphical processors for a probable optimization of computational time for simulations on more refined grids.

References

Al-Rawahi, N. and G. Tryggvason (2004). Numerical simulation of dendritic solidification with convection: Three-dimensional flow. *Journal of Computational Physics 194*(2), 677–696.

Ammerman, C. N., S. M. You, and Y. S. Hong (1996). Identification of pool boiling heat transfer mechanisms from a wire immersed in saturated fc-72 using a single-photo/lda method. *Journal of Heat Transfer 118*, 117–123.

Anderson, D. M., G. B. McFadden, and A. A. Wheeler (1998). Diffuse-interface methods in fluid mechanics. *Annual Review of Fluid Mechanics 30*(1), 139–165.

Attinger, D., Z. Zhao, and D. Poulikakos (2000). An experimental study of molten microdroplet surface deposition and solidification: Transient behavior and wetting angle dynamics. *Journal of Heat Trasnfer 122*(3), 544–556.

Besant, W. H. (1859). *A Treatise on Hydrostatics and Hydrodynamics*. Cambridge: Deighton Bell.

Borges, R., M. Carmona, B. Costa, and W. S. Don (2008). An improved weighted essentially non-oscillatory scheme for hyperbolic conservation laws. *Journal of Computational Physics 227*(6), 3191–3211.

Chatzikyriakou, D., S. P. Walker, G. F. Hewitt, C. Narayanan, and D. Lakehal (2009). Comparison of measured and modelled droplet-hot wall interactions. *Applied Thermal Engineering 29*, 1398–1405.

Chorin, A. J. (1968). Numerical solution of the navier-stokes equations. *Mathematics of Computation 22*(104), 745–762.

Clift, R., J. R. Grace, and M. E. Weber (2005). *Bubbles, Drops, and Particles*. Dover Civil and Mechanical Engineering Series. Dover Publications.

Drew, D. A. (1983). Mathematical modeling of two-phase flow. *Annual Review of Fluid Mechanics 15*(1), 261–291.

Drew, D. A. and R. T. Lahey, Jr (1993). Analytical modeling of multiphase flow. *Particulate Two-Phase Flow 17*, 509–566.

Esmaeeli, A. and G. Tryggvason (2003). Computations of explosive boiling in microgravity. *Journal of Scientific Computing 19*, 163–182.

Esmaeeli, A. and G. Tryggvason (2004). Computations of film boiling. part i: Numerical method. *International Journal of Heat and Mass Transfer 47*(25), 5451–5461.

Farooqi, M. N., D. Izbassarov, M. Muradoğlu, and D. Unat (2019). Communication analysis and optimization of 3d front tracking method for multiphase flow simulations. *The International Journal of High Performance Computing Applications 33*(1), 67–80.

Fedkiw, R. P., T. Aslam, B. Merriman, and S. Osher (1999). A non-oscillatory eulerian approach to interfaces in multimaterial flows (the ghost fluid method). *Journal of Computational Physics 152*(2), 457–492.

Frigo, M. and S. G. Johnson (2005). The design and implementation of FFTW3. *Proceedings of the IEEE 93*(2), 216–231.

Ge, Y. and L.-S. Fan (2006). 3-d modeling of the dynamics and heat transfer characteristics of subcooled droplet impact on a surface with film boiling. *International Journal of Heat and Mass Transfer 49*, 4231–4249.

Gibou, F., L. Chen, D. Nguyen, and S. Banerjee (2007). A level set based sharp interface method for the multiphase incompressible navier-stokes equations with phase change. *Journal of Computational Physics 222*(2), 536–555.

Glimm, J., E. Isaacson, D. Marchesin, and O. McBryan (1981). Front tracking for hyperbolic systems. *Advances in Applied Mathematics 2*(1), 91–119.

Glimm, J., D. Marchesin, and O. McBryan (1981). A numerical method for two-phase flow with an unstable interface. *Journal of Computational Physics 39*(1), 179–200.

Glimm, J. and O. A. McBryan (1985). A computational model for interfaces. *Advances in Applied Mathematics 6*(4), 422–435.

Gordillo, J. and G. Riboux (2022). The initial impact of drops cushioned by an air or vapour layer with applications to the dynamic leidenfrost regime. *Journal of Fluid Mechanics 941*, A10.

Groberg, Z. B. (2001). Respiratory fluid mechanics and transport processes. *Annual Review of Biomedical Engineering 3*(1), 421–457.

Harlow, F. H. and J. E. Welch (1965). Numerical calculation of time-dependent viscous incompressible flow of fluid with free surface. *Physics of Fluids 8*(12), 2182–2189.

Harvie, D. J. E. and D. F. Fletcher (2001). A hydrodynamic and thermodynamic simulation of droplet impacts on hot surfaces, part i: Theoretical model. *International Journal of Heat and Mass Transfer 44*, 2633–2642.

Hirt, C. and B. Nichols (1981). Volume of fluid (vof) method for the dynamics of free boundaries. *Journal of Computational Physics 39*(1), 201–225.

Irfan, M. and M. Muradoglu (2017). A front tracking method for direct numerical simulation of evaporation process in a multiphase system. *Journal of Computational Physics 337*, 132–153.

Irfan, M. and M. Muradoglu (2018). A front tracking method for particle-resolved simulation of evaporation and combustion of a fuel droplet. *Computers & Fluids 174*, 283–299.

Ishii, M. (1987). Interfacial area modeling. *Multiphase Science and Technology 3*, 31–61.

Jacqmin, D. (1999). Calculation of two-phase navier-stokes flows using phase-field modeling. *Journal of Computational Physics 155*(1), 96–127.

Juric, D. and G. Tryggvason (1998). Computations of boiling flows. *International Journal of Multiphase Flow 24*(3), 387–410.

Kamakoti, R. and W. Shyy (2004). Fluid-structure interaction for aeroelastic applications. *Progress in Aerospace Sciences 40*, 535–558.

Karami, N., M. H. Rahimian, and M. Farhadzadeh (2017). Numerical simulation of droplet evaporation on a hot surface near leidenfrost regime using multiphase lattice boltzmann method. *Applied Mathematics and Computation 312*(C), 91–108.

Karl, A., K. Anders, M. Rieber, and A. Frohn (1996). Deformation of liquid droplets during collisions with hot walls: Experimental and numerical results. *Particle & Particle Systems Characterization 13*, 186–191.

Kim, J. (2007). Spray cooling heat transfer: The state of the art. *International Journal of Heat and Fluid Flow 28*(4), 753–767.

Larson, R. G., H. T. Davis, and L. E. Scriven (1981). Displacement of residual nonwetting fluid from porous media. *Chemical Engineering Scince 36*(1), 75–85.

Lee, H. S. (1993). *Vapor bubble dynamics in microgravity.* Ph. D. thesis, The University of Michigan.

Lee, T. (2009). Effects of incompressibility on the elimination of parasitic currents in the lattice boltzmann equation method for binary fluids. *Computers & Mathematics with Applications 58*, 987–994.

Leidenfrost, G. (1756). *De Aquae Communis Nonnullis Qualitatibus Tractatus.* Ovenius.

Leonard, B. P. (1979). A stable and accurate convective modelling procedure based on quadratic upstream interpolation. *Computer Methods in Applied Mechanics and Engineering 19*(1), 59.

Mikic, B. B., W. M. Rohsenow, and P. Griffith (1970). On bubble growth rate. *International Journal of Heat and Mass Transfer 13*(4), 657–666.

Mittal, R. and G. Iaccarino (2005). Immersed boundary method. *Annual Review of Fluid Mechanics 37*, 239–261.

Moreira, A. L. N., A. S. Moita, and M. R. Panão (2010). Advances and challenges in explaining fuel spray impingement: How much of single droplet impact research is useful? *Progress in Energy and Combustion Science 36*(5), 554–580.

Muradoglu, M. and G. Tryggvason (2008). A front-tracking method for computation of interfacial flows with soluble surfactants. *Journal of Computational Physics 227*(4), 2238–2262.

Muradoglu, M. and G. Tryggvason (2014). Simulations of soluble surfactants in 3d multiphase flow. *Journal of Computational Physics 274*, 737–757.

Nas, S., M. Muradoglu, and G. Tryggvason (2006). Pattern formation of drops in thermocapillary migration. *International Journal of Heat and Mass Transfer 49*(13), 2265–2276.

Naseer, H. U., Z. Ahmed, D. Izbassarov, and M. Muradoglu (2023). Dynamics and interactions of parallel bubbles rising in a viscoelastic fluid under buoyancy. *Journal of Non-Newtonian Fluid Mechanics 313*, 105000.

Nomura, H., Y. Ujiie, H. J. Rath, J. Sato, and M. Kono (1996). Experimental study on high-pressure droplet evaporation using microgravity conditions. *Symposium (International) on Combustion 26*(1), 1267–1273.

Olbricht, W. L. (1996). Pore-scale prototypes of multiphase flow in porous media. *Annual Review of Fluid Mechanics 28*(1), 187–213.

Osher, S. and J. A. Sethian (1988). Fronts propagating with curvature-dependent speed: Algorithms based on hamilton-jacobi formulations. *Journal of Computational Physics 79*, 12–49.

Peskin, C. S. (1977). Numerical analysis of blood flow in the heart. *Journal of Computational Physics 25*(3), 220–252.

Plesset, M. S. and S. A. Zwick (1954). The growth of vapor bubbles in superheated liquids. *Journal of Applied Physics 25*(4), 493–500.

Pournaderi, P. and A. R. Pishevar (2012). A numerical investigation of droplet impact on a heated wall in the film boiling regime. *Heat and Mass Transfer 48*, 1525–1538.

Prosperetti, A. and M. S. Plesset (1978). Vapour-bubble growth in a superheated liquid. *Journal of Fluid Mechanics 85*(2), 349–368.

Qian, J., G. Tryggvason, and C. Law (1998). A front tracking method for the motion of premixed flames. *Journal of Computational Physics 144*(1), 52–69.

Rayleigh, L. (1917). On the pressure developed in a liquid during the collapse of a spherical cavity. *Philosophical Magazine 34*, 94–98.

Safari, H., M. H. Rahimian, and M. Krafczyk (2013). Extended lattice boltzmann method for numerical simulation of thermal phase change in two-phase fluid flow. *Physical Review E 88*, 013304.

Safari, H., M. H. Rahimian, and M. Krafczyk (2014). Consistent simulation of droplet evaporation based on the phase-field multiphase lattice boltzmann method. *Physical Review E 90*, 033305.

Schlottke, J. and B. Weigand (2008). Direct numerical simulation of evaporating droplets. *Journal of Computational Physics 227*(10), 5215–5237.

Son, G. and V. Dhir (1998). Numerical simulation of film boiling near critical pressures with a level set method. *ASME Journal of Heat and Mass Transfer 120*(1), 183–192.

Sussman, M., P. Smereka, and S. Osher (1994). A level set approach for computing solutions to incompressible two-phase flow. *Journal of Computational Physics 114*(1), 146–159.

Tanguy, S., T. Menard, and A. Berlemont (2007). A level set method for vaporizing two-phase flows. *Journal of Computational Physics 221*(2), 837–853.

Tryggvason, G., B. Bunner, A. Esmaeeli, D. Juric, N. Al-Rawahi, W. Tauber, J. Han, S. Nas, and Y.-J. Jan (2001). A front-tracking method for the computations of multiphase flow. *Journal of Computational Physics 169*(2), 708–759.

Tryggvason, G., R. Scardovelli, and S. Zaleski (2011). *Direct Numerical Simulations of Gas-Liquid Multiphase Flows*. Cambridge University Press.

Udaykumar, H. S., W. Shyy, and M. M. Rao (1996). Elafint: a mixed Eulerian-Lagrangian method for fluid flows with complex and moving boundaries. *International Journal for Numerical Methods in Fluids 22*(8), 691–712.

Unverdi, S. O. and G. Tryggvason (1992). A front-tracking method for viscous, incompressible, multi-fluid flows. *Journal of Computational Physics 100*(1), 25–37.

Welch, S. W. and J. Wilson (2000). A volume-of-fluid based method for fluid flows with phase change. *Journal of Computational Physics 160*(2), 662–682.

Woerner, M. (2012). Numerical modeling of multiphase flows in microfluidics and micro process engineering: a review of methods and applications. *Microfluidics and Nanofluidics 12*(6), 841–886.

Zhang, D. Z. and A. Prosperetti (1994). Ensemble phase-averaged equations for bubbly flows. *Physics of Fluids 6*(9), 2956–2970.

Zhang, H. (2004). Numerical research on a vaporizing fuel droplet in a forced convective environment. *International Journal of Multiphase Flow 30*(2), 181–198.